# DESIGN, ANALYSES AND EXPERIMENTAL STUDY OF A FOIL GAS BEARING WITH COMPRESSION SPRINGS AS A COMPLIANT SUPPORT

A Thesis

by

JU HO SONG

Submitted to the Office of Graduate Studies of
Texas A&M University
in partial fulfillment of the requirements for the degree of

MASTER OF SCIENCE

August 2006

Major Subject: Mechanical Engineering

# DESIGN, ANALYSES AND EXPERIMENTAL STUDY OF A FOIL GAS BEARING WITH COMPRESSION SPRINGS AS A COMPLIANT SUPPORT

A Thesis

by

JU HO SONG

Submitted to the Office of Graduate Studies of
Texas A&M University
in partial fulfillment of the requirements for the degree of

MASTER OF SCIENCE

Approved by:

| | |
|---|---|
| Chair of Committee, | Daejong Kim |
| Committee Members, | Luis San Andrés<br>Wayne N.P. Hung |
| Head of Department, | Dennis O'Neal |

August 2006

Major Subject: Mechanical Engineering

# ABSTRACT

Design, Analyses and Experimental Study of a Foil Gas Bearing with Compression Springs as a Compliance Support. (August 2006)

Ju Ho Song, B.S., Korea University

Chair of Advisory Committee: Dr. Daejong Kim

A new foil bearing with compression springs is designed, built, analyzed, and tested. This foil gas bearing uses a series of compression springs as a compliant structure instead of corrugated bump foils. A spring model to estimate the stiffness of compression springs was developed and showed a good level of agreement with the experimental results. The spring dynamics model was combined with a non-linear orbit simulation to investigate the non-linear behavior of foil gas bearings. The approach could also predict the structural loss factor given the geometry of the underlying springs.

A series of rotor-bearing orbit simulations using the compression spring with stiffness of the free-free case, predicted the critical speed and the onset speed of instability at around 7500 rpm and 14,500 rpm with a WFR ~ 0.5. The low critical speed was due to the relatively soft support. The hydrodynamic rotor instability was predicted under the equivalent viscous damping extracted from the spring dynamics, implying the viscous damping alone within the spring cannot suppress hydrodynamic instability of the foil gas bearings.

The load capacity of the compression spring foil gas bearing was measured at 20,000 rpm with and without air cooling, to demonstrate the feasibility of the new foil bearing. The constructed bearing with rather soft springs showed a small load capacity of 96N at 20,000 rpm under no cooling. The developed cooling method using direct air supply holes machined on the bearing sleeve, proved to be very effective in cooling the test bearing. The measured level of structural stiffness and damping evidenced the existence of a necessary level of damping for stable bearing operation. The structural stiffness was highly nonlinear and showed different behavior for static loading and the sinusoidal dynamic loading. The measured equivalent viscous damping coefficients increased with the applied load amplitude.

A series of parametric design studies were performed to investigate the effects of various design parameters on the bearing stiffness and overall rotordynamic performance. Rotor-bearing orbit simulations showed there is a range of spring stiffness for high onset

speeds of instability. Increasing the pitch of the spring while maintaining the same stiffness increased the structural loss factor slightly, manifesting a smaller number of coils is better in terms of damping. The onset speed of instability increases slightly with the rotor mass due to increased static eccentricity and presumably smaller cross-coupled stiffness. However, increasing the rotor mass in order to render a high eccentricity was not effective in increasing the onset speed of instability because of reduced natural frequency and increased inertia. Instead, orbit simulations confirmed that small rotor mass with external loading is the most effective way to increase the bearing stability.

# DEDICATION

This thesis is dedicated to God and my family for their endless love and sacrifice.

# ACKNOWLEDGMENTS

I would like to thank Dr. Kim for his academic supervision and support during my graduate research. Sincere thanks to Dr. Luis San Andrés and Dr. Wayne N.P. Hung for their valuable recommendation and consideration as committee members. I also appreciate the assistance of Mr. Eddy Denk for his assistance on test rig construction. A special thanks to Seung gook Park for his help on the experiments. The devotion and help from my friends, Taeho Kim, Kyuho Sim, Keun Ryu, Anthony Breedlove and many others is really appreciated. Finally I would like to finish my acknowledgment by expressing endless thanks and love to God and my family.

# TABLE OF CONTENTS

Page

# LIST OF FIGURES

Page

Page

Page

# LIST OF TABLES

Page

# NOMENCLATURE

| | |
|---|---|
| $T_i$ | Vertical force of $i^{th}$ spring coil |
| $F_i$ | Horizontal force of $i^{th}$ spring coil |
| $F_{Tfi}$ | Friction force between spring and top foil |
| $F_{Bfi}$ | Friction force between spring and bearing sleeve |
| $M$ | Total moment |
| $M_{bi}$ | Bending moment of $i^{th}$ spring coil |
| $M_{ti}$ | Torsion of $i^{th}$ spring coil |
| $M_0$ | Moment at top of $i^{th}$ spring coil |
| $B_i$ | Reaction force at bearing sleeve |
| $\alpha$ | Vertical force coefficient |
| $\beta$ | Ratio of reaction force on right support (Equation 15) |
| $\vec{r}$ | Position vector |
| $\theta$ | Angular coordinate (Figure III.3 (a)) |
| $\phi$ | Angular coordinate ( $= 2\pi - \theta$ ) (Figure III.3 (b)) |
| $\vec{n}$ , $\vec{n}'$ | Unit normal vector of $\vec{r}$ and $\vec{r}'$ |
| $l$ | Spring pitch |
| $a$ | Spring radius |
| $EI$ | Bending rigidity |
| $GJ$ | Torsional rigidity |
| $U$ | Total elastic stored energy within a spring |
| $\mu$ | Friction coefficient between spring and sleeve |
| $\eta$ | Friction coefficient between top foil and spring |
| $w_i$ | Vertical deflection of $i^{th}$ spring coil |
| $W_i$ | Non-dimensional vertical deflection of $i^{th}$ spring coil |
| $u_i$ | Slip of $i^{th}$ spring coil against top foil |

| | |
|---|---|
| $v_i$ | Slip of i$^{th}$ spring coil against bearing sleeve |
| $S_i$ | Total slip of i$^{th}$ spring coil against bearing sleeve |
| $D_i$ | Total slip of i$^{th}$ spring coil against top foil |
| $U_{Ci}$ | Dissipated energy by Coulomb friction |
| $k_i$ | Stiffness of i$^{th}$ spring |
| $f_i$ | Compliance of i$^{th}$ spring |
| $f_{Di}$ | Equivalent Coulomb friction force |
| $b_i$ | Equivalent viscous damping coefficient of i$^{th}$ spring |
| $\omega$ | Angular velocity |
| $C$ | Nominal bearing clearance of foil gas bearing |
| $R$ | Bearing radius |
| $h$ | Local gas film thickness |
| $H$ | Non-dimensional film thickness |
| $e$ | Journal eccentricity |
| $\varepsilon$ | Non-dimensional eccentricity ( = $e/C$ ) |
| $p$ | Pressure |
| $P$ | Non-dimensional pressure ( = $p/p_a$ ) |
| $Z$ | Non-dimensional axial coordinate ( = $z/R$ ) |
| $\tau$ | Non-dimensional time ( = $\omega t$ ) |
| $\Lambda$ | Bearing number |
| $\sigma$ | Squeeze number |
| $m$ | Rotor mass |
| $m_u$ | Imbalance mass |
| $F_e$ | Total external forces |
| $F_b$ | Bearing reaction forces |
| $T_0$ | Amplitude of vertical dynamic load |
| $W_0$ | Amplitude of vertical deflection |

| | |
|---|---|
| $k^*$ | Complex stiffness |
| $\gamma$ | Structural loss factor |
| $k$ | Stiffness of one compression spring |
| $M_{sys}$ | System mass of the bearing |
| $K$ | Dynamic structural stiffness of the bearing |
| $F(t)$ | Sinusoidal Excitation Force |
| $F_0$ | Amplitude of dynamic load, $F(t)$ |
| $Z(\omega)$ | Mechanical impedance of system |
| $F_C$ | Coulomb friction force |
| $C_{eq}$ | Equivalent viscous damping coefficient of the bearing |
| $\Delta E_C$ | Energy dissipated from Coulomb damping |
| $\Delta E_V$ | Energy dissipated from viscous damping |
| $W_{sys}$ | Work performed by the excitation force |

## Subscripts

| | |
|---|---|
| $R$ | Right hand side of spring |
| $L$ | left hand side of spring |

# CHAPTER I

# INTRODUCTION

Oil lubricated rolling element bearings are widely used to support rotors in gas turbines, because these bearings have large load capacity and predictable performance. However, oil lubrication circuits make the system complicated and environmentally unfriendly. In midsized turbomachinery, foil gas bearings can offer an alternative solution, making the system light and compact, improving reliability. For these reasons, foil gas bearings have been developed for decades.

Foil gas bearings are one of the hydrodynamic bearings which employ the self-generating pressure when a rotor spins. Figure I.1 shows a typical configuration of bump foil gas bearings with a corrugated bump foil and smooth top foil. The bump foil supports the top foil to provide the structural stiffness, and hydrodynamic pressure is generated in the clearance between the top foil and rotating rotor. The bump foil and top foil layers are welded at one end, and the other end is free to move.

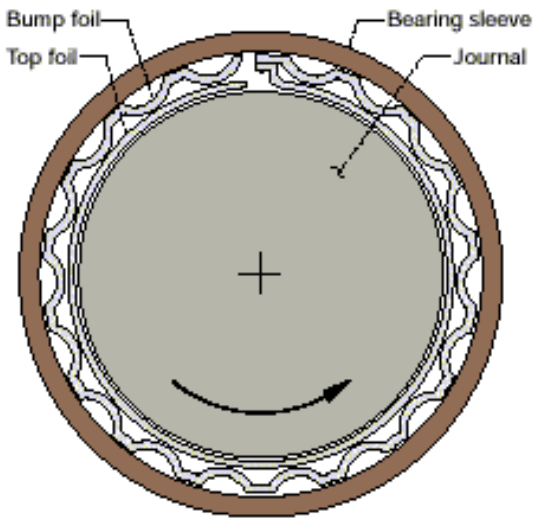


**Figure I.1 Schematic view of foil gas bearing [1]**

This thesis follows the style of ASME Journal of Tribology.

While it is stationary, the rotor sits on the top foil, rendering deflection of the bump foil and forms a wedge shape between the top foil and rotor. When the rotor starts to spin, hydrodynamic pressure is generated from the wedge, lifting the rotor to be completely airborne. The bump foil deforms elastically according to the generated pressure and friction of the bearing becomes very small. Because of this compliant bump foil structure, foil gas bearings can effectively accommodate misalignment and rotor growth (both centrifugal and thermal). In addition, bump foil gas bearings use any gas as a working and cooling fluid, there is no need for additional lubrication mechanisms, thus enabling the construction fo a compact and maintenance-free system.

Current applications of gas bearings include auxiliary power units (APU), air management systems for aircraft [2], micro-gas turbines (MGT) as independent power generators or for fuel cell-MGT hybrid systems [3], turbochargers, turbo compressors, etc.

## 1.1 Literature Review

Heshmat et al [4] preformed the first numerical analysis of bump foil gas bearings with a uniform bump stiffness assumption. He solved the Reynolds Equation using finite element methods and evaluated the pressure distribution, load capacity, and drag of foil gas bearings. In addition, he showed that foil gas bearings have a higher load capacity than conventional gas bearings for a given film thickness.

Ku and Heshmat [5] presented an analytical model predicting the deformation of a bump foil. The total elastic bending moment within the bump foils was evaluated by treating the friction forces as conservative forces. Their model predicts a higher stiffness if a frictional force is introduced between the bumps and the bearing sleeve and/or the top foil. The bumps near the fixed end have a higher stiffness than the bumps near the free end. In the following paper, Ku and Heshmat examined the bump deflection to verify their analytical model, as presented in [5]. They used an optical tracking device to measure the bump deflection and the recorded hysteresis loops of the bump foil indicated Coulomb damping between the bump foil and the contacting surfaces. In addition, they presented the bump stiffness versus applied loads curves in order to show the effect of bump geometry on stiffness.

Peng and Carpino [6] adopted the bending moment equation given in [5] and used

an energy method to calculate slip and equivalent viscous damping coefficients under conditions of pure sinusoidal excitation. Peng and Carpino [7] also predicted the stiffness and damping coefficients of foil gas bearings, employing a perturbation and finite element methods. In their analysis, predicted stiffness increases with the rotor speed and decreases with the compliance of the bump foil. At low speeds, the overall bearing stiffness depends on the generated hydrodynamic pressure. However, at high speeds, the overall bearing stiffness relies on the structural stiffness of the bump foil, because the stiffness of the hydrodynamic film is very high. The effect of bearing compliance on the dynamic force coefficients is presented as well.

Iordanoff [8] introduced a simple method to design foil gas thrust bearings. He used a composite profile consisting of a constant slope in the leading edge and a parallel surface to the bearing runner.

Heshmat [9] introduced a bump foil gas bearing which uses a multi-layered bump foil to increase the load capacity. This bearing successfully reached the very high operating speed of 132,000 rpm and showed a large load capacity of nearly 100psi at 60krpm.

DellaCorte et al [10] introduced a simple “rule of thumb” method for predicting load capacities of foil gas bearings as compared to rigid wall bearings based on many tests results.

Dykas and Howard [11] advanced understanding of thermal runaway of foil gas bearings that can happen in even lightly loaded cases involving undesirable rotor geometry and a thermal gradient of the rotor.

Radil et al [12] investigated the effects of radial clearance on the load capacity. They showed that a very small clearance without adequate cooling can lead to thermal runway, i.e., film rupture and a reduced bearing load capacity, On the contrary, a foil gas bearing with twice the optimum clearance had a slightly decreased load capacity without any thermal problems.

Kim and San Andrés [13] advanced general understanding of foil gas bearings through analytical predictions (via isothermal gas bearing theory) of load capacity and dynamic force coefficients as a function of structural stiffness and loss factor of bump foils. They predicted a bearing stiffness close to the bump structural stiffness for heavily loaded foil bearings, manifesting a very large stiffness of air film. Kim and San Andrés [14] also showed that the maximum load capacity of foil gas bearings are determined mainly by the maximum allowable structural deflection of the underlying support

structure if thermal effects are neglected.

Heshmat and Ku [15] presented an experimental method to measure the dynamic structural stiffness and damping of foil gas bearings. They used a stationary shaft and an electromagnet shaker to excite the test foil gas bearing in X and Y directions. The structural stiffness and equivalent viscous damping coefficients were evaluated from the force equilibrium equations on the shaft, showing that they have a decreasing tendency with increasing dynamic loads. In the same paper, Heshmat and Ku presented that direct damping terms decrease with the excitation frequency.

Rubio and San Andrés [16] advance an experimental method to identify the structural stiffness and damping of bump foil gas bearings. Authors employed a frequency domain analysis of mechanical impedance to measure the dynamic structural stiffness and equivalent viscous damping coefficient of foil gas bearing. They presented that the dynamic structural stiffness showed hardening effect with decreased dynamic loads due to stick slip phenomenon. In addition, identified equivalent viscous damping coefficients are frequency dependant and increased with the magnitude of applied dynamic loads, especially for excitation below the system natural frequency.

# CHAPTER II

# RESEARCH OBJECTIVE

The basic operating principle of bump foil bearings lies in the underlying compliant bump structure that provides stiffness and damping. Therefore, foil gas bearings can be designed with any support structure providing adequate stiffness and damping to the top foil. To better understand the general behavior of foil gas bearings in a laboratory environment, a simple support structure with predictable stiffness and damping characteristics is desirable. Moreover, for the parametric studies on design parameters such as stiffness distribution, bearing clearance, and overall top foil morphology (i.e., circular, preloaded, etc), it is necessary to have a foil gas bearing with design parameters that are adjustable and tunable with minimal effort. Keeping these factors in mind, a simple foil gas bearing with compression springs was designed as shown in Figure II.1. The bearing sleeve has multiple circular slots along the circumferential direction in which the compression springs are inserted along the axial direction.

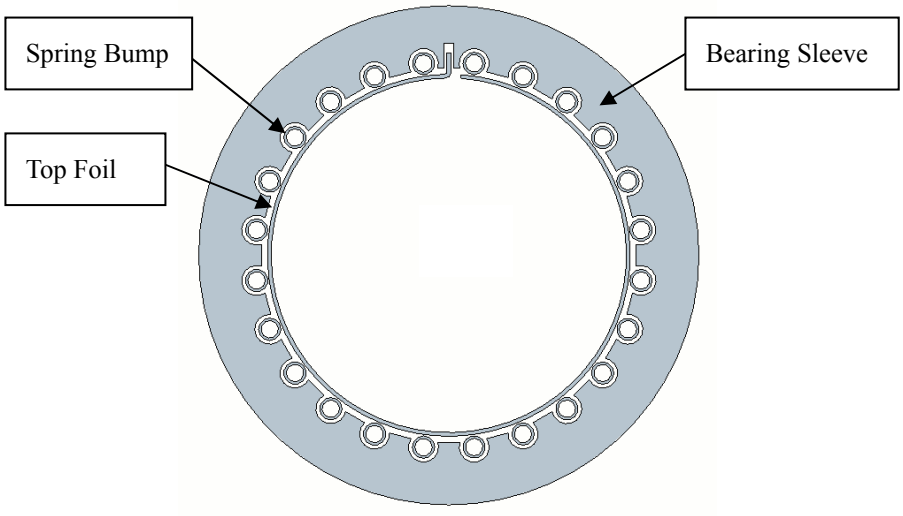


**Figure II.1 Schematic view of foil gas bearing with compression springs**

In this configuration, the compression springs are under side loading, and the axial stretching of the springs and the friction between the springs and the bearing sleeve generates the necessary Coulomb damping. The stiffness can be tuned by simply exchanging the springs with others of different wire diameters, maintaining the same overall diameter. Any damaged springs can be exchanged by simply putting in a new one. Furthermore, the bearing can be transformed to a preloaded one by inserting springs with a different overall diameter into the selected slots. To facilitate the aforementioned advantages, an accurate analytical model to predict spring stiffness should be made available.

The main objectives of this research are (1) to develop an analytical model to predict the spring stiffness and damping; (2) to develop a unified approach for investigating the non-linear behavior of foil gas bearings using rotor-bearing orbit simulations combined with spring dynamics; (3) to prove the concept of compression spring foil gas bearings by measuring load capacity, structural stiffness, and damping; (4) to perform parametric studies on design parameters to achieve spring stiffness and damping comparable to those of conventional bump foil bearings.

## 2.1 Description of Foil Gas Bearing with Compression Springs

Figure II.2 shows photos of a novel foil gas bearing supported by multiple compression springs arranged along the axial direction. The stainless steel bearing sleeve was made by wire-electro discharge machining (EDM) process. Commercially available stainless steel compression springs were inserted into the circular axial slots to provide the support stiffness and Coulomb damping that traditional bump foils provide. The wire diameter, pitch and overall diameter of the springs are 0.254mm, 3.42mm, and 2.90mm, respectively.

The top foil of the bearing was made from stainless steel, through a hot forming process. Stainless steel foil was inserted into the top foil forming jig (as seen in Figure A.2). The top foil foaming jig was heated to 650°C and then maintained for 8 hours in a nitrogen gas environment.

Two thin aluminum end plates cover the both ends of the bearing sleeve to prevent the springs from slipping out of the slots. Low friction Diamond-Like Carbon (DLC) was applied to the bearing sleeve to facilitate easy movement of the spring s. The inside

surface of the top foil was coated with Teflon, but the backside was left a bare surface. Table II.1 shows more detailed specifications for the foil gas bearing with compression springs.

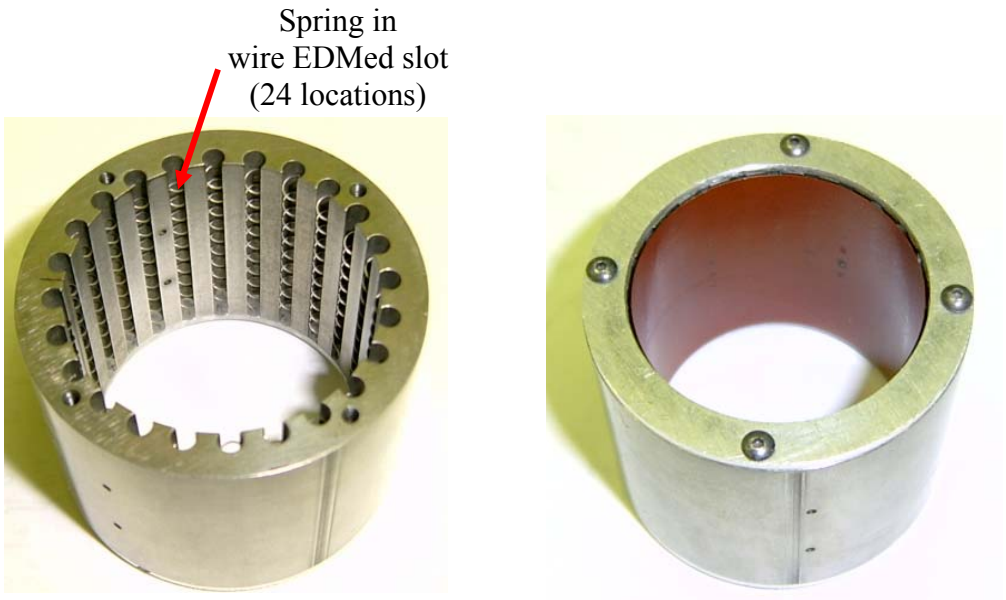


(a) With top foil removed (b) Assembled foil bearing

**Figure II.2 Photo of foil gas bearing with compression springs**

**Table II.1 Parameters for new foil gas bearing and springs**

| Foil gas bearing parameters | | |
|---|---|---|
| **Parameters** | **SI Units** | **English Units** |
| Inner diameter | 38.10 mm | 1.50 inch |
| Outer diameter | 50.80 mm | 2.00 inch |
| Axial length | 38.10 mm | 1.50 inch |
| Nominal clearance | 45.0 ± 0.8 μm | 1.77 ± 0.33 mil |
| Number of springs | 24 | |

**Table II.1 continued**

| Foil gas bearing parameters | | |
|---|---|---|
| Top foil thickness | 0.102 mm | 0.004 inch (4mil ) |
| Top foil coating | 25.4 μm Teflon | 0.001 inch Teflon |
| Sleeve groove coating | Diamond-Like Carbon (DLC) | |
| Spring parameters | | |
| Spring length | 30.00 mm | 1.180 inch |
| Spring pitch | 3.33 mm | 0.131 inch |
| Spring diameter | 2.90 mm | 0.114 inch |
| Spring wire diameter | 0.254 mm | 0.010 inch |

# CHAPTER III

# SIMULATION OF FOIL GAS BEARING WITH COMPRESSION SPRINGS

## 3.1 Spring Simulation

### 3.1.1 Analysis of Compression Springs

To calculate the stiffness and damping coefficients of compression springs in the foil gas bearing, Castigliano's energy method was employed. Cartesian coordinates were used to analyze the spring element using the parametric variable $\theta$, as seen in Figure III.1.

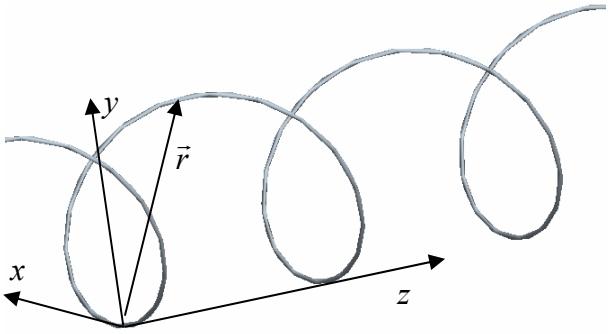


(a) 3-D view of springs

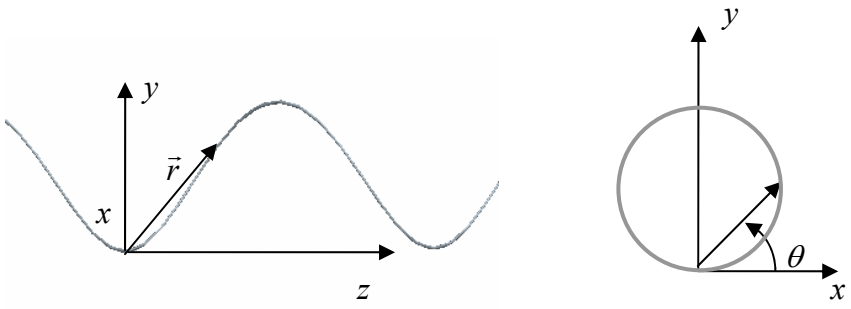


(b) Side and axial view of springs with definition of $\theta$

**Figure III.1 Coordinate system for analyses of springs**

As shown for bump type foil gas bearings [6], the equivalent viscous damping coefficients of bumps near the fixed end are smaller than those of bumps near the free end. Because the suggested compression spring foil gas bearing consists of multiple springs arranged along the axial direction, the spring element at the center of the bearing can be assumed to be fixed, and both ends are free to move. To simplify the modeling process, each spring pitch was modeled as a single spring coil interacting with other spring coils through friction and transmitted forces from adjacent spring coils (as seen in Figure III.2).

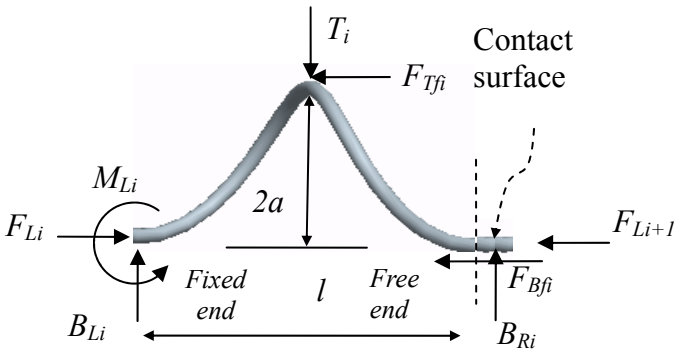


(a) Free body diagram of one complete spring coil

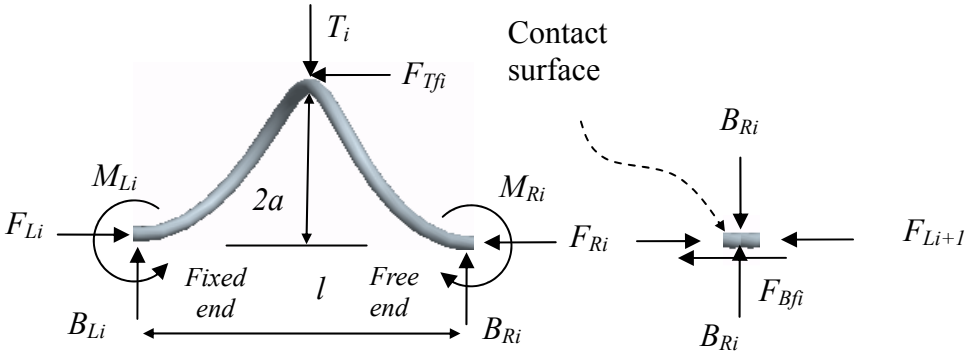


(b) Free body diagram of one spring coil excluding contact area

**Figure III.2 Free body diagram of spring coil**

In this model, the left hand side of the spring coil does not have a sliding interface with the bearing sleeve and all the sliding interfaces are assigned to the right hand side of the spring coil.

Initially, assuming both ends pinned condition (allowing no movement), the reaction force to the spring coil $F_{Ri}^{S}$ (or thrust force to the contact area) can be evaluated for load $T_i$. If $F_{Ri}^{S} < \mu_S B_{Ri} + F_{Li+1}$, the $i^{th}$ spring coil is pinned and no movement is allowed. On the other hands, if $F_{Ri}^{S} \geq \mu_S B_{Ri} + F_{Li+1}$, the $i^{th}$ spring coil begins to move and a new force equilibrium on the curved spring coil is established as follows (neglecting the inertia of the spring), and can be seen in Figure III.2 (b),

$$F_{Li} = F_{Ri} + F_{Tfi} = F_{Li+1} + F_{Bfi} + F_{Tfi} \qquad (i=1,\ldots,m) \tag{1}$$

where $F_{Tfi} = \eta T_i$ and $F_{Bfi} = \mu T_i$ are friction forces from the top foil and bearing sleeve, respectively. $\eta$ and $\mu$ are kinetic friction coefficients of the spring/top foil interface and the spring/bearing sleeve interface, respectively. In the free body diagram shown in Figure III.2 (b), $F_{Bfi}$ is not applied to the curved spring coil because the friction force is applied only to the small contact area, shown as a short horizontal line on the right hand side of the vertical dotted line in Figure III.2 (a). The effect of the friction force to the curved spring coil appears in $F_{Ri}$ which is identical in magnitude but opposite in direction to the summation of the friction force ($F_{Bfi}$) and transmitted forces ($F_{Li+1}$) from $i+1^{th}$ to $m^{th}$ spring coils. Even if all the friction forces are not conservative forces, these friction forces are assumed to contribute to the bending moment when the spring coil is moving. At the end of the $m^{th}$ spring coil, $F_{Lm+1}$ =0 and all the $F_{Li}$ can be calculated using the recursive formula given in Equation (1).

An estimation of the stiffness of the new foil gas bearings employs 3-dimensional analyses on the bending moment and torsion. From the moment equilibrium of the entire spring coil, shown on the left hand side of Figure III.2 (b),

$$M_{Ri} = M_{Li} - T_i \frac{l}{2} + 2aF_{Tfi} + B_{Ri} l \tag{2}$$

Because actual spring is continuous, $M_{Ri} = M_{Li+1}$ and $M_{Rm} = 0$ at the last spring bump. Force equilibrium in $z$ direction states

$$F_{Li} = F_{Ri} + F_{Tfi} \tag{3}$$

Force equilibrium in *y* direction becomes

$$T_i = B_{Li} + B_{Ri} \tag{4}$$

From Equations (2) and (4), it can be seen that the reaction forces from the bearing sleeves are

$$B_{Li} = \alpha T_i + \frac{M_{Li} - M_{Ri}}{l} \tag{5.a}$$

$$B_{Ri} = (1-\alpha) T_i - \frac{M_{Li} - M_{Ri}}{l} \tag{5.b}$$

where $\alpha = \frac{1}{2} + \frac{2a\eta}{l}$.

As seen in Figure III.3, the spring coil is divided into two regions, namely, $0 \le \theta \le \pi$ and $\pi < \theta \le 2\pi$.

1) $0 \le \theta \le \pi$

A vector leading to the position of interest necessary to evaluate the total moment [as seen in Figure III.3 (a)] is given by

$$\vec{r} = a\sin\theta\vec{i} + a(1-\cos\theta)\vec{j} + \frac{l\theta}{2\pi}\vec{k} \tag{6}$$

where 2*a* and *p* are the overall diameter of the spring and the pitch, respectively. From the moment balance with all the external forces in the free body diagram,

$$\vec{M}_L = \left( M_{Li} + a(1-\cos\theta)F_{Li} - \frac{l\theta}{2\pi}B_{Li} \right)\vec{i} + a\sin\theta F_{Li}\vec{j} - a\sin\theta B_{Li}\vec{k} \tag{7}$$

2) $\pi < \theta \le 2\pi$

In this region [seen in Figure III.3 (b)], a new parameter $\phi = 2\pi - \theta$ is used to define the position vector. Because of the geometrical nature of the continuous coil springs, when the spring is observed from the right hand side, the rotational sense of the coil is exactly identical to that of the left hand side ( $0 \le \theta \le \pi$ ). Therefore,

$$\vec{r}'(\phi) = a\sin\phi\,\vec{i}' + a(1-\cos\phi)\vec{j}' + \frac{l\phi}{2\pi}\vec{k}' \tag{8}$$

and,

$$\vec{M}_R = \left( M_{Ri} + a(1-\cos\phi)F_{Ri} - \frac{l\phi}{2\pi}B_{Ri} \right)\vec{i}' + a\sin\phi F_{Ri}\vec{j}' + a\sin\phi B_{Ri}\vec{k}' \tag{9}$$

Note that the friction force $F_{TFi}\,(=\eta T_i)$ does not explicitly appear in either Equation (7) or (9) because the friction force is already included implicitly in Equation (7) through the force equilibrium in $z$ direction made available through Equation (3).

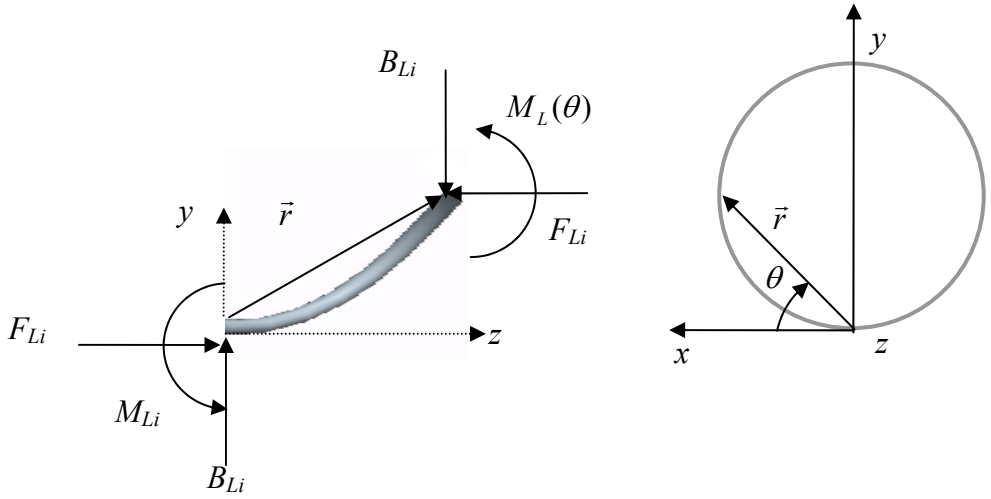


(a) $0 \le \theta \le \pi$

**Figure III.3 Free body diagram of partial spring coil**

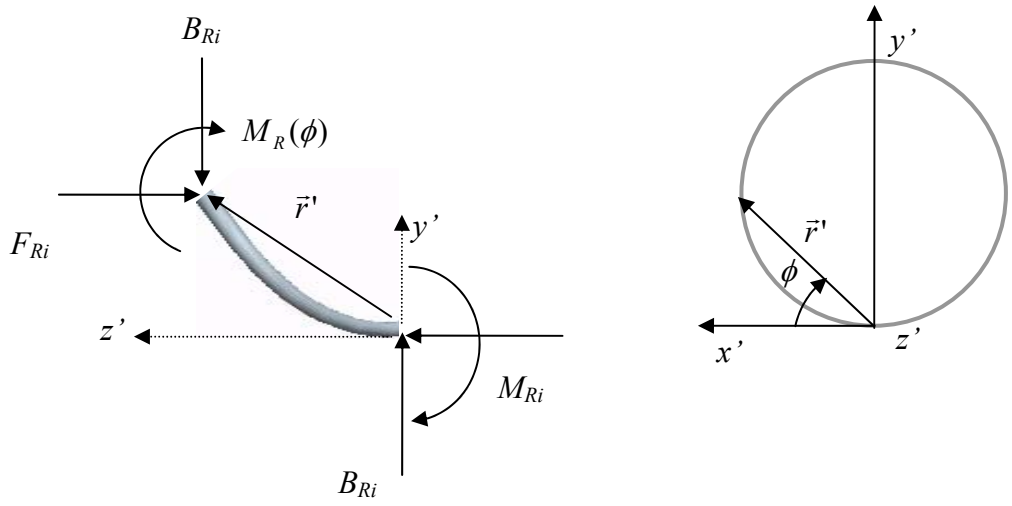


(b) $0 \le \phi \le \pi$

**Fig III.3 Continued**

Because the total moment vector applied to the coil section is three-dimensional, the moment vector should be decomposed into the bending moment and the torsion in order to calculate the total elastic energy. As seen in Figure III.4, Unit normal vectors at $\vec{r}$ and $\vec{r}'$ are given by the following equations:

$$\vec{n} = \frac{d\vec{r}}{|d\vec{r}|} = \frac{1}{\sqrt{1+\left(\frac{l}{2\pi a}\right)^2}}\left(\cos\theta\vec{i} + \sin\theta\vec{j} + \frac{l}{2\pi a}\vec{k}\right) \tag{10.a}$$

$$\vec{n}' = \frac{d\vec{r}'}{|d\vec{r}'|} = \frac{1}{\sqrt{1+\left(\frac{l}{2\pi a}\right)^2}}\left(\cos\phi\vec{i}' + \sin\phi\vec{j}' + \frac{l}{2\pi a}\vec{k}'\right) \tag{10.b}$$

As seen in Figure III.4, the torsion and the bending moment on the spring become

$$\vec{M}_{tL} = \left(\vec{n}\cdot\vec{M}_L\right)\vec{n} \tag{11.a}$$

$$\vec{M}_{tR} = \left(\vec{n}' \cdot \vec{M}_R\right)\vec{n}' \tag{11.b}$$

$$\vec{M}_{bL} = \vec{M}_L - \vec{T}_L \tag{11.c}$$

$$\vec{M}_{bR} = \vec{M}_R - \vec{T}_R \tag{11.d}$$

and the total strain energy stored in the spring element becomes

$$U = \int_0^{\pi}\left(\frac{M_{bL}^{\ 2}}{2EI} + \frac{\vec{M}_{tL}^{\ 2}}{2GJ}\right)\left|d\vec{r}\right| + \int_0^{\pi}\left(\frac{M_{bR}^{\ 2}}{2EI} + \frac{\vec{M}_{tR}^{\ 2}}{2GJ}\right)\left|d\vec{r}'\right| \tag{12}$$

where $\left|d\vec{r}\right| = a\sqrt{1+\left(\frac{l}{2\pi a}\right)^2}\,d\theta$ and $\left|d\vec{r}'\right| = a\sqrt{1+\left(\frac{l}{2\pi a}\right)^2}\,d\phi$.

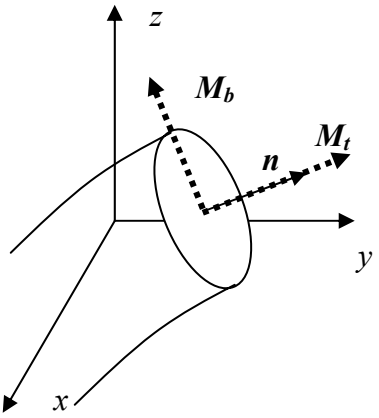


**Figure III.4 Definition of normal vector for decomposition of total moment into bending and torsion**

The unknown moments $M_{Li}$ and $M_{Ri}$ in Equations (7) and (9) can be calculated from geometrical and kinetic constraints on top of the spring coil and at the free end.

From Equations (7) or (9), the moment at the top of the spring coil ($\theta = \pi$ or $\phi = \pi$) should be equal, .i.e.,

$$M_0\big|_{\theta=\pi} = M_{Li} + 2aF_{Li} - \frac{l}{2}B_{Li} \tag{13.a}$$

$$M_0\big|_{\phi=\pi} = M_{Ri} + 2aF_{Ri} - \frac{l}{2}B_{Ri} \tag{13.b}$$

Other equations necessary to solve for the unknowns come from the geometrical constraints at the top and the free end of the spring coil. Equation (12) representing the total strain energy, as a function of $M_o$ and reaction forces appearing in the Figure III.3 (b) and imposing a zero slope on the top of the spring coil, i.e., $\frac{\partial U}{\partial M_0} = 0$,

$$M_0 = aF_{Ri} + \frac{a}{2}F_{Tfi} - \frac{l}{8}B_{Ri} \tag{14}$$

Imposing another boundary condition, $\frac{\partial U}{\partial B_{Ri}} = 0$,

$$B_{Ri} = \beta T_i \tag{15.a}$$

$$B_{Li} = T_i - B_{Ri} = (1-\beta)T_i \tag{15.b}$$

where $\beta = \left(EIA_1 + GJA_2\right)/\left(EIA_3 + GJA_4\right)$. The expression for constants $A_{\text{i=1,2,3,4}}$ are given in the APPENDIX B**.** An interesting result is that both $B_{Li}$ and $B_{Ri}$ are functions of only $T_i$ and friction coefficient $\eta$. Combining this knowledge with Equations (13) and (14) using Equation (15), yields

$$M_{Li} = aF_{Ri} + \frac{a}{2}F_{Tfi} - \frac{l}{8}B_{Ri} - 2aF_{Li} + \frac{l}{2}B_{Li} \tag{16.a}$$

$$M_{Ri} = -aF_{Ri} + \frac{a}{2}F_{Tfi} + \frac{3l}{8}B_{Ri} \tag{16.b}$$

Because of all the unknowns are solved, the total strain energy of the spring can be evaluated using Equation (12). Any vertical deflection and/or horizontal slips against the top foil and bearing sleeve can be evaluated using Castigliano's theorem [17]. The vertical deflection of top foil yields:

$$\frac{\partial U}{\partial T_i} = w_i \tag{17}$$

The horizontal slip of the spring against the bearing sleeve leads to:

$$\frac{\partial U}{\partial F_{Ri}} = v_i = -a\frac{E_1 T_i + E_2 F_{Ri}}{2\pi^2 EIGJ\sqrt{l^2 + 4a^2\pi^2}} \tag{18}$$

The horizontal slip of the spring against the top foil leads to:

$$\frac{\partial U}{\partial F_{Tfi}} = u_i = -a\frac{M_1 T_i + M_2 F_{Ri}}{16\pi^2 EIGJ\sqrt{l^2 + 4a^2\pi^2}} \tag{19}$$

Expressions for $E_1$, $E_2$, $M_1$, and $M_2$ are given in APPENDIX B.

### 3.1.2 Spring Dynamics

Spring dynamics can be represented as

$$T_i = k_i w_i + f_{Di} \tag{20}$$

, where $k_i$ is a spring stiffness and $f_{Di}$ is the total equivalent Coulomb friction force in the direction of $w_i$ from all the sliding interfaces. Expressions for the stiffness and equivalent Coulomb friction force can be found by rewriting Equation (17) as:

$$w_i = \frac{\partial U}{\partial T_i} = f_i T_i - g_{Di} \tag{21.a}$$

or

$$T_i = \frac{w_i}{f_i} + \frac{g_{Di}}{f_i} \tag{21.b}$$

Here, $g_{Di}$ is a damping force in the vertical deflection $w_i$. Comparing Equations (20) and (21), the stiffness $k_i$, equivalent friction force $f_{Di}$, and the compliance $f_i$ are given as

$$k_i = 1/f_i = \frac{192EIGJ\sqrt{l^2 + 4a^2\pi^2}}{D_1 + D_2} \tag{22.a}$$

$$f_{Di} = g_{Di}/f_i = \frac{12(C_1 F_{Ri} + C_2 \eta T_i)}{\pi^2 (D_1 + D_2)} \tag{22.b}$$

$$f_i = H_1 EI + H_2 GJ \tag{23}$$

Expressions for $C_1$, $C_2$, $D_1$, $D_2$, $H_1$ and $H_2$ are given in APPENDIX B.

As can be shown from equation (23), the compliance comes from two effects, i.e., bending ($EI$) and torsion ($GJ$). From equation (22.a), $k_i$ is a function of only geometrical and material parameters of the spring, and contains only the friction coefficient $\eta$ (not $\mu$) through the parameter $\beta$. Note that the parameter $\beta$ distributes the vertical reaction forces, which are conservative forces supporting the spring. All the contributions of the tangential friction forces ($F_{Tfi}=\eta T_i$ and $F_{Bfi}=\mu B_{Ri}$) appear in the equivalent damping force (22.b). Because $\beta \approx 0.48$~$0.49$ for wide range of $\eta$, the stiffness given by Equation (22.a) is almost identical to the case of free sliding case ($\beta$=0.5). Physically it is true because any additional resistance of the spring deflection from the dry frictions contributes to the damping force. Therefore, when sliding occurs to a spring under friction, the stiffness of the spring takes the value for the free sliding case.

### 3.1.3 Dissipative Energy from Dry Friction

In Figure III.2, the slip of the $i^{th}$ spring coil comes from two contributions, i.e., a local slip, given as (18) and (19) generated by load $T_i$ and a global slip of the $i^{th}$ spring coil transmitted from upstream spring coils. As seen in Figure III.5, the total slip of the $i^{th}$ spring coil against the top foil becomes

$$D_i = S_{i-1} + u \tag{24.a}$$

$$D_1 = u_1 \tag{24.b}$$

where the total slip of each spring coil can be evaluated using

$$S_i = S_{i-1} + v_i \tag{25.a}$$

$$S_1 = v_1 \tag{25.b}$$

When the top foil has been deflected as $w_i$ under dynamic load $T_i$, the Coulomb friction energy can be calculated by multiplying Equations (24) and (25) with associated friction forces,

$$U_{Ci} = F_{Tfi} \cdot D_i + F_{Bfi} \cdot S_i \tag{26}$$

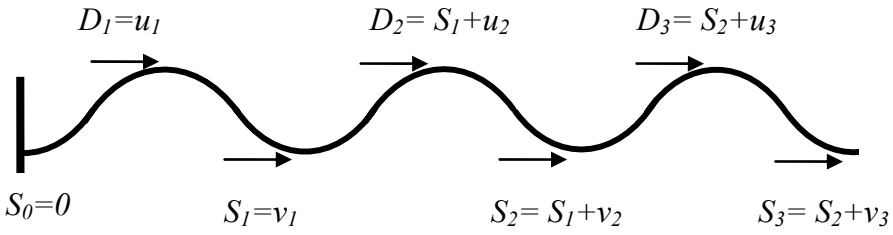


**Figure III.5 Description of global slip of continuous spring coils**

Even if the damping in the foil gas bearings comes from Coulomb friction, the equivalent viscous damping coefficient of each spring is evaluated for the orbit

simulations (as shown in section 3.2 and Chapter V). The spring-viscous damper model can be written as,

$$T_i = k_i w_i + b_i \dot{w}_i \tag{27}$$

where $b_i$ is an equivalent viscous damping coefficient. The $k_i$ was assumed constant because the spring is deflected within linear ranges. During the $T_i$ loading, the dissipated friction energy should be equal to the equivalent viscous damping energy. If the pressure load $T_i$ is changed from $T_i^{n-1}$ to $T_i^n$ over $dt$, the change of Coulomb friction energy becomes:

$$dU_{Ci}{}^n = U_{Ci}{}^n - U_{Ci}{}^{n-1} \tag{28}$$

The change of equivalent viscous damping energy over the $dt$ should become:

$$dU_{Vi}{}^n = b_i{}^n \dot{w}_i{}^n \cdot dw_i{}^n \cong b_i{}^n \left( \frac{dw_i{}^n}{dt} \right)^2 dt \tag{29}$$

Equating Equations (28) and (29) yields:

$$b_i{}^n = \left| \frac{\dfrac{dU_{Ci}}{dt}}{\left( \dfrac{dw_i}{dt} \right)^2} \right|^n \tag{30}$$

Time derivatives were approximated using finite difference formula in the time domain. Plugging Equations (30) into (27) and non-dimensionalizing yields:

$$\frac{T_i{}^n}{k_i C} = W_i{}^n + \frac{b_i{}^n \omega}{k_i} \dot{W}_i{}^n \tag{31}$$

where dot is a derivative with respect to the non-dimensional time $\tau = \omega t$.

### 3.2 Rotor-Bearing Orbit Simulation

#### 3.2.1 Dynamic Analysis of Foil Gas Bearing with Compression Springs

The dynamic performance of the foil gas bearing was evaluated using a rotor-bearing orbit method. This orbit method shows the path of the rotor center by simultaneously solving the journal dynamics and Reynolds equation.

Considering the deflection of the spring, the non-dimensional film thickness is given by

$$H = 1 + \varepsilon_X \cos\theta + \varepsilon_Y \sin\theta + W(\theta, Z) \tag{32}$$

where $W(\theta)$ is a local spring deflection normalized by nominal bearing clearance, i.e. $W(\theta) = w(\theta)/C$. Under the synchronous imbalance excitation, the pressure on the top foil is also a time-varying function. If the spring inertia is neglected, the spring dynamic Equations (20) and (27) can be applied to dynamically loaded cases such as the imbalance responses. In the orbit simulation, the dynamic pressure force is used with Equation (31) to calculate the spring deflection at each time step. The averaged equivalent viscous damping coefficient of all the springs was used to simplify the analysis and save computational time.

Dynamic bearing reaction forces to the journal can be obtained by solving Reynolds Equation with an assumption of isothermal continuum flow.

$$\frac{\partial}{\partial\theta}\left(PH^3\frac{\partial P}{\partial\theta}\right) + \frac{\partial}{\partial Z}\left(PH^3\frac{\partial P}{\partial Z}\right) = \Lambda\frac{\partial(PH)}{\partial\theta} + \sigma\frac{\partial(PH)}{\partial\tau} \tag{33}$$

where

$$P = p/p_a \tag{33.a}$$
$$\theta = x/R \tag{33.b}$$
$$Z = z/R \tag{33.c}$$
$$H = h/C \tag{33.d}$$
$$\tau = \omega t \tag{33.e}$$
$$\varepsilon = e/C \tag{33.f}$$

Here $p_a$ is the atmospheric pressure, $R$ is a bearing radius and $C$ is a bearing clearance. In the Equation (33), $\Lambda$ is a bearing number and $\sigma$ is a squeeze number defined as

$$\Lambda = \frac{6\mu\omega}{p_a}\left(\frac{R}{C}\right)^2 \tag{34.a}$$

$$\sigma = \frac{12\mu\omega}{p_a}\left(\frac{R}{C}\right)^2 \tag{34.b}$$

Once the pressure filed $P(\theta, Z)$ is obtained from the Reynolds equations, the bearing reaction force to the rotor can be calculated as

$$F_{bX} = -p_a R^2 \int_0^{2\pi}\int_0^{L/R} (P(\theta,Z)-1)\cos\theta \; d\theta \; dZ \tag{35.a}$$

$$F_{bY} = -p_a R^2 \int_0^{2\pi}\int_0^{L/R} (P(\theta,Z)-1)\sin\theta \; d\theta \; dZ \tag{35.b}$$

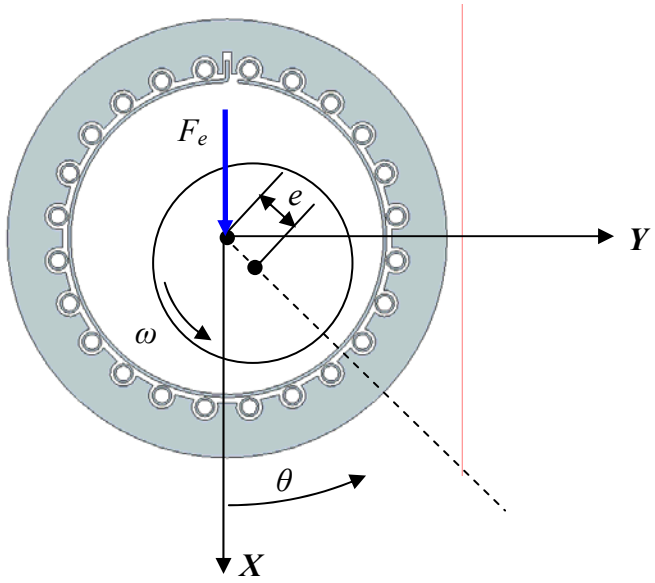


**Figure III.6 Free body diagram of foil gas bearing at equilibrium point**

Equations which express the rotor motions of the foil gas bearing shown in Figure III.6 can be written by

$$m_r C\omega^2 \frac{d^2\varepsilon_X}{d\tau^2} = F_{bX} + F_{eX} \tag{36.a}$$

$$m_r C\omega^2 \frac{d^2\varepsilon_Y}{d\tau^2} = F_{bY} + F_{eY} \tag{36.b}$$

where $F_{bX,Y}$ are bearing reaction forces in $X$ and $Y$ directions and $F_{eX,Y}$ are total external forces in $X$ and $Y$ directions including the rotor weight and imbalance force, which can be expressed as

$$F_{eX} = m_u R\omega^2 \cos\tau + m_r g \tag{37.a}$$

$$F_{eY} = m_u R\omega^2 \sin\tau \tag{37.b}$$

At the equilibrium point, external forces $F_{eX,Y}$ and bearing reaction forces $F_{bX,Y}$ are the same in amplitude, but opposite in direction.

### 3.2.2 Scheme for Numerical Analysis

If four state variables are defined as

$$\varepsilon_X = X_1 \tag{38.a}$$
$$\dot{\varepsilon}_X = X_2 \tag{38.b}$$
$$\varepsilon_Y = X_3 \tag{38.c}$$
$$\dot{\varepsilon}_Y = X_4 \tag{38.d}$$

then Equation (36) can be expressed as four 1st order differential equations, i.e.,

$$\dot{X}_1 = X_2 \tag{39.a}$$

$$\dot{X}_2 = \frac{F_{eX} + F_{bX}}{m_r C \omega^2} \tag{39.b}$$

$$\dot{X}_3 = X_4 \tag{39.c}$$

$$\dot{X}_4 = \frac{F_{eY} + F_{bY}}{m_r C \omega^2} \tag{39.d}$$

The four differential equations are numerically integrated in time domain in order to calculate the traces of the rotor center. Because Equation (31) is defined for every computational grid point, treatment of $W(\theta)$ as a state variable requires as many state equations as the number of computational grid points. To save computational time, the following explicit method is used. $P^{(n)}$ is calculated using $W^{(n-1)}$. Once $P^{(n)}$ is calculated, $W^{(n)}$ is evaluated to define $H^{(n+1)}$ and successive $P^{(n+1)}$. Choosing a fine time step (720 non-dimensional time steps for one rotation) can minimize error involved with the explicit scheme.

A fifth order Adams-Bashforth scheme [18] defined as

$$X_i^{n+1} = X_i^n + \frac{\Delta t}{720}(1901 f_i^n - 2774 f_i^{n-1} + 2616 f_i^{n-2} - 1274 f_i^{n-3} + 251 f_i^{n-4}) \tag{40}$$

was used for the numerical time integration to evaluate the state variables. State variables for the first five steps were calculated using a fourth order Runge Kutta method. The advantage of Adams-Bashforth scheme over Runge Kutta method is a single evaluation of the function at each time step, instead of four separate calculations. Figure III.7 shows the flow chart of the orbit simulation. The number of computational grid points to solve the Reynolds Equation is 72×11.

In the forthcoming rotor-bearing orbit simulations, all parameters are selected to simulate the actual imbalance response test conditions. An imbalance of 570 mg-mm was chosen based on the preliminary simulations that show clear and discernable circular obits for stable conditions. The rotor mass is half of the actual rotor manufactured for imbalance response tests. The friction coefficients $\mu$ (DLC coating) and $\eta$ (bare steel surface) are chosen as 0.1 and 0.5, respectively, from the coating supplier's specification and the material data book [19]. The bearing clearance for simulations is 25 μm. Simulation parameters with other design variables are summarized in Table III.1.

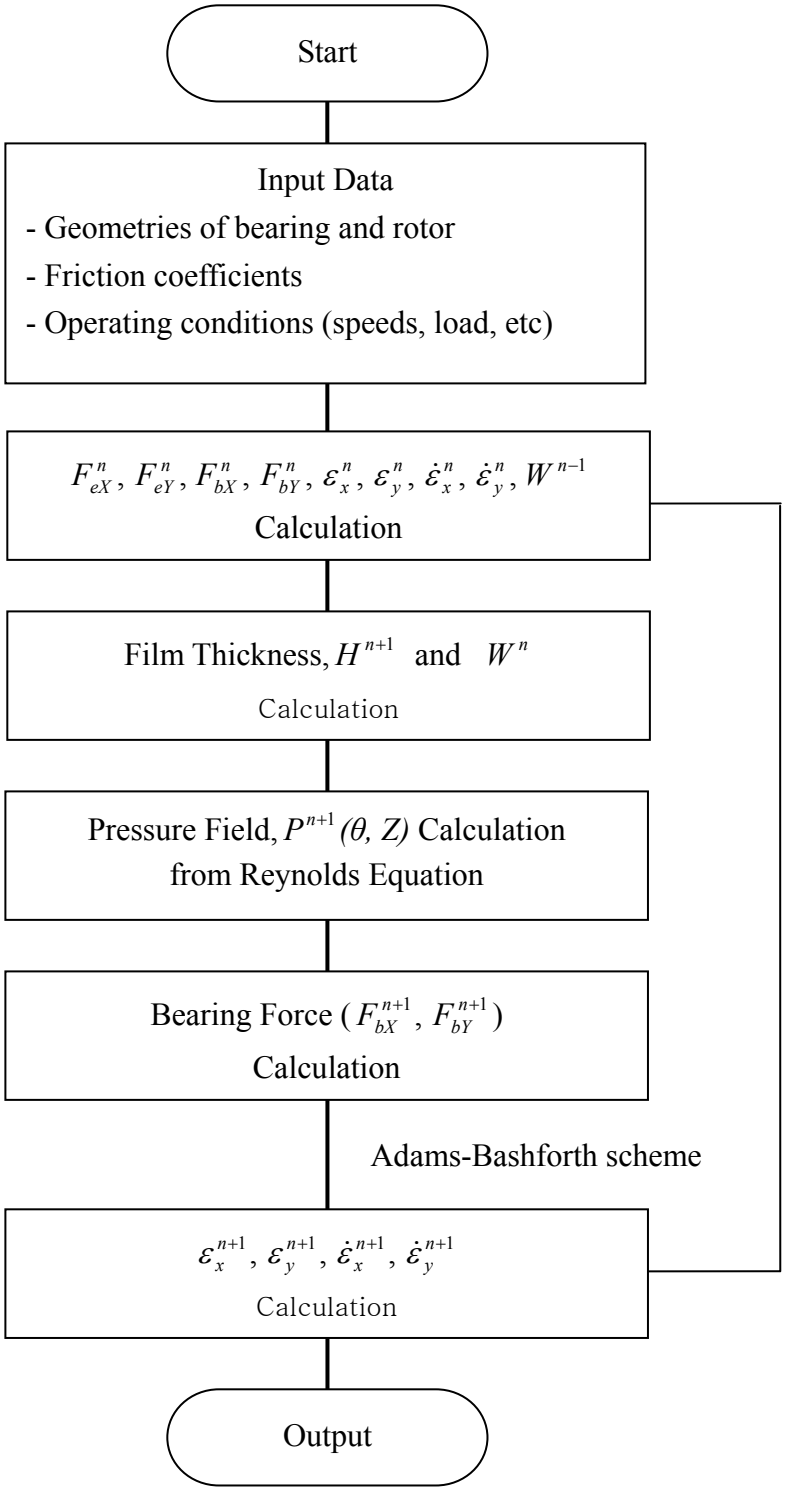


**Figure III.7 Flow chart of orbit simulation**

**Table III.1 Parameters for orbit simulation**

| | |
|---|---|
| Unbalance mass, $m_u$ | 570 mg-mm |
| Rotor mass, $m$ | 0.60 kg |
| Friction coefficient between spring and sleeve, $\mu$ | 0.1 |
| Friction coefficient between spring and top foil, $\eta$ | 0.5 |
| Wire diameter of spring, $r$ | 0.254 mm |
| Spring pitch, $p$ | 3.42 mm |
| Spring radius, $a$ | 1.45 mm |
| Nominal clearance, $C$ | 0.025 mm |

### 3.2.3 Results of Rotor-Bearing Orbit Simulation

A series of rotor-bearing orbit simulations were performed to determine the imbalance responses of the rotor. As seen in Figure III.8, rotordynamic instability of the foil gas bearing occurs at around 14,500 rpm, with a whirl frequency ratio of near 0.5.

Figure III.9 shows the predicted amplitude and phase angle of rotor-bearing imbalance responses. The phase angle is between the direction of imbalance and the rotor displacement in $X$ direction. The natural frequency of the foil gas bearing appears at around 7,500 rpm and critical speed is about 8,500 rpm (critical speeds along the Y and X axes are 7,500 and 9,000 rpm, respectively). A modal damping ratio can be estimated roughly as 0.25 from the imbalance response when phase angle is 90° from Figure III.9.

The developed spring dynamic model (as seen in Section 3.1.3) can predict structural loss factor (i.e., damping) of underling springs once the spring geometry and friction coefficients are given.

A single degree of freedom (SDOF) spring-damper model of the top foil and spring (with negligible inertia) under a dynamic excitation force, *T(t)* can be defined as:

$$b\dot{w}(t) + kw(t) = T(t) \tag{41}$$

Assume $w(t) = W_0 e^{i\omega t}$ and $T(t) = T_0 e^{i\omega t}$, then

$$(k + ib\omega)W_0 = k\left(1 + i\frac{b\omega}{k}\right)X = T_0 \tag{42.a}$$

or

$$k^* W_0 = T_0 \tag{42.b}$$

where $k^* = k(1+\gamma i)$ is a complex stiffness and $\gamma = b\omega/k$ is s defined as a structural loss factor. It shows that a spring viscous damper under sinusoidal excitation can be modeled as a complex stiffness (i.e. impedance). The structural loss factor is related to the amount of energy dissipation of the system and it is defined for only sinusoidal steady state response [20].

Figure III.10 is a cyclic variation of an averaged (over all the springs) structural loss factor at 12,000rpm. The time-averaged structural loss factor from Figure III.10 is 0.228 and very close to many empirical observations from other experimental studies on bump foil gas bearings [5, 12, 13, 17].

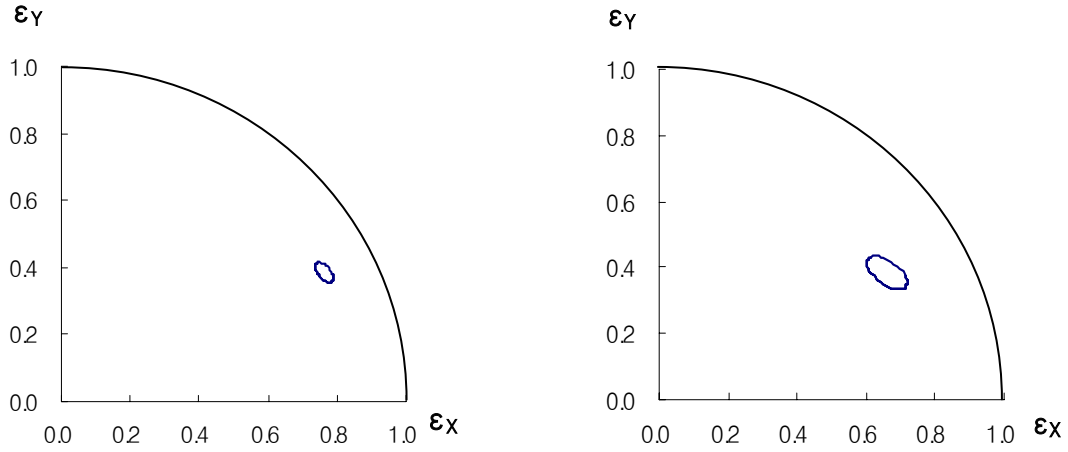


(a) 5,000rpm (b) 7,000rpm

**Figure III.8 Simulated rotor-bearing imbalance responses (static load is applied in $\varepsilon_X$ direction)**

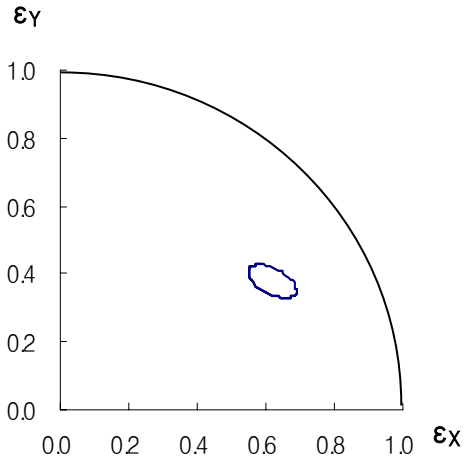


(c) 8,000rpm

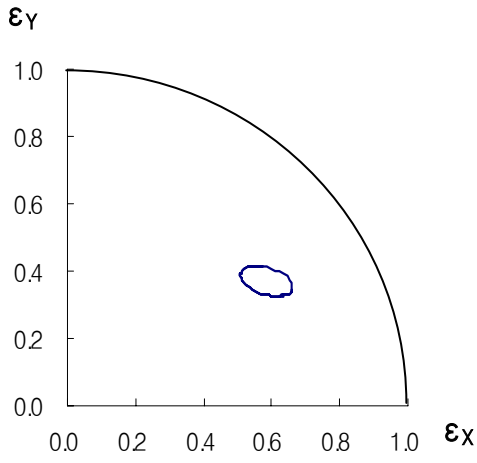


(d) 9,000rpm

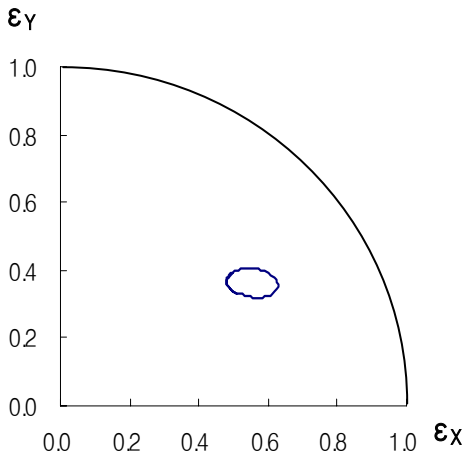


(c) 10,000rpm

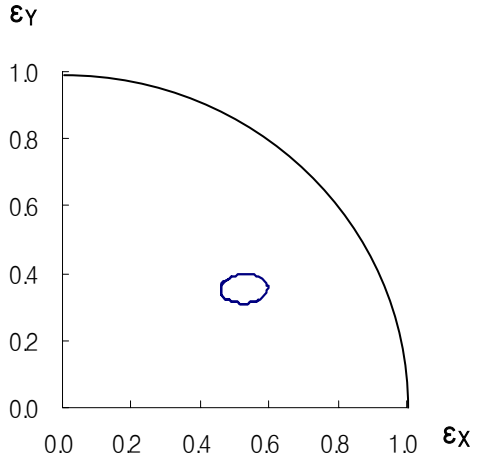


(d) 11,000rpm

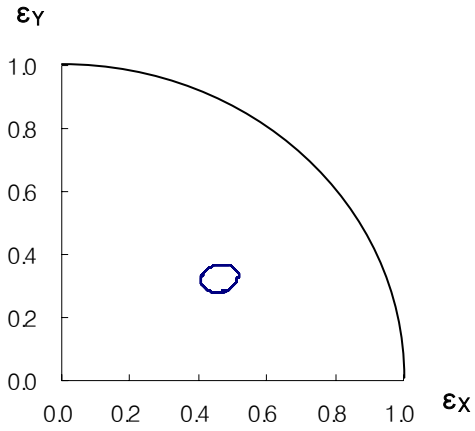


(e) 14,000rpm

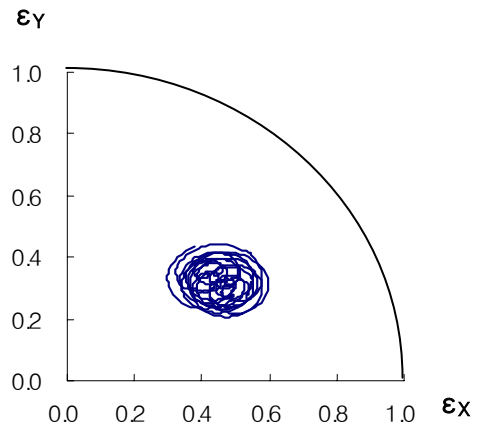


(f) 14,500rpm

**Figure III.8 Continued**

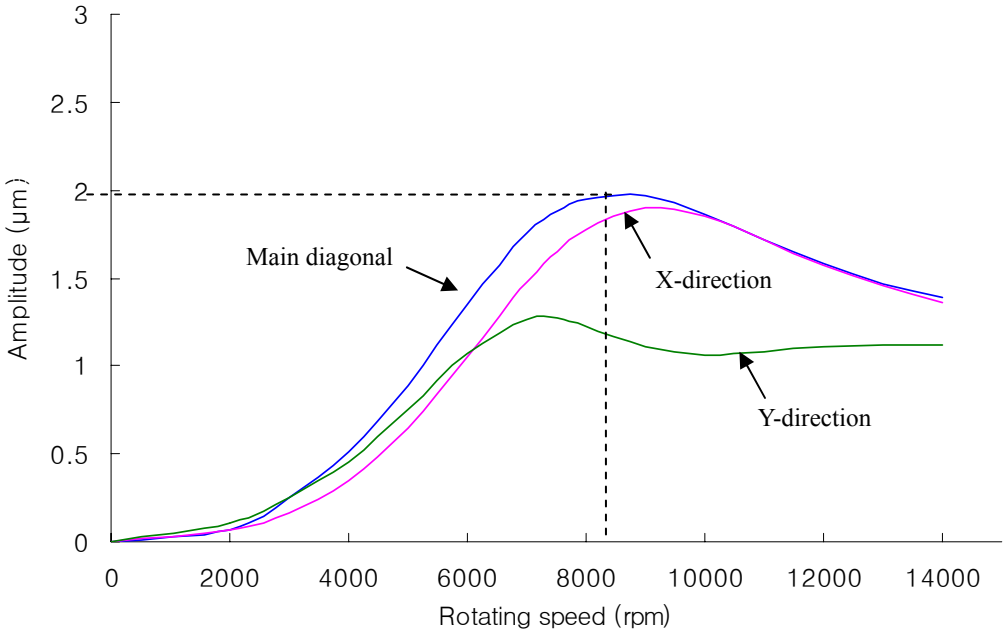


(a) Amplitude of orbit versus rotating speed

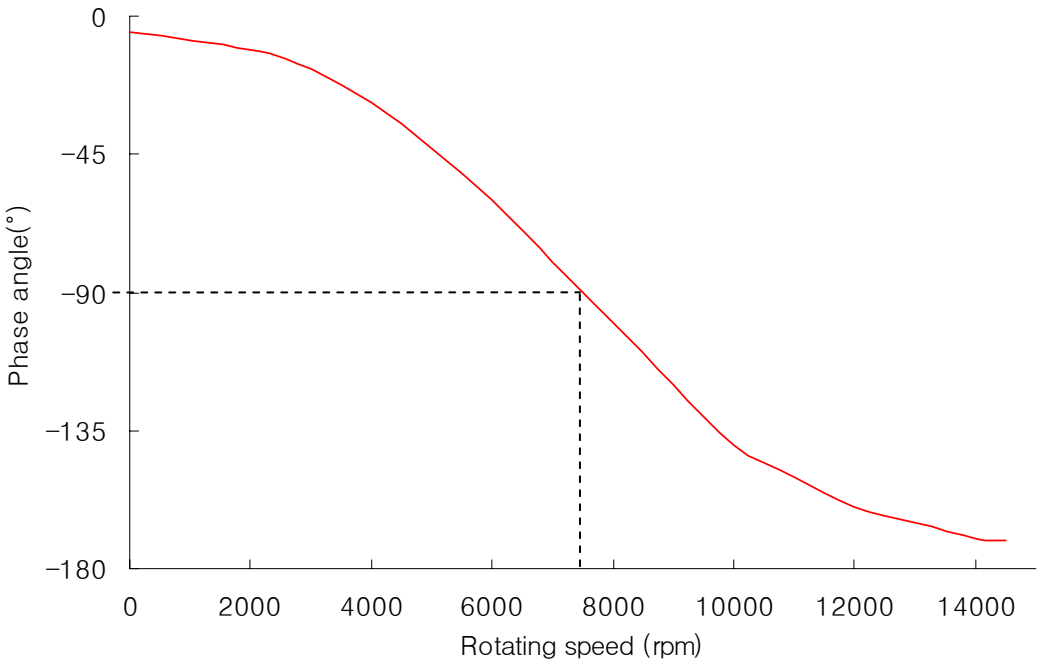


(b) Phase angle versus rotating speed

**Figure III.9 Simulated amplitude and phase angle of rotor-bearing imbalance responses with rotating speed**

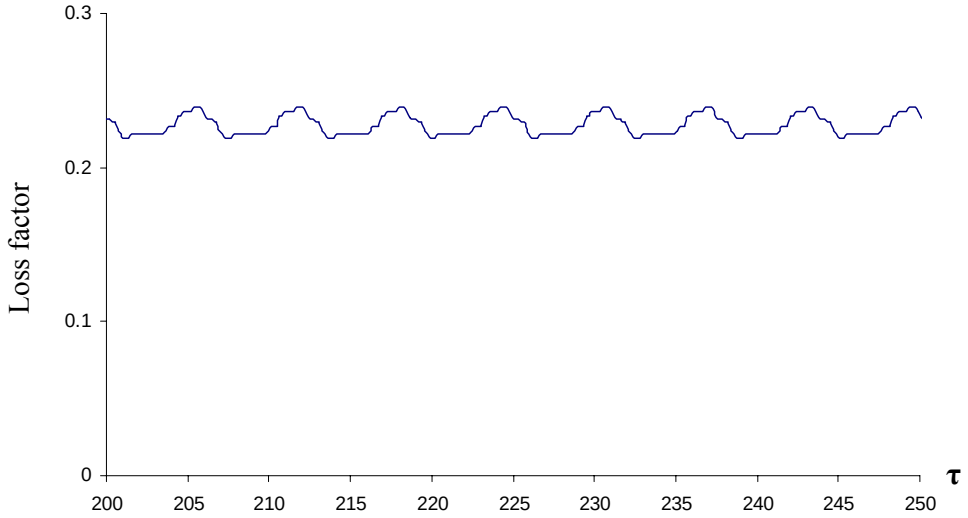


**Figure III.10 Simulated cyclic variation of structural loss factor**

# CHAPTER IV

# EXPERIMENTS OF FOIL GAS BEARING WITH COMPRESSION SPRINGS

## 4.1 Spring Stiffness Measurements

### 4.1.1 Experimental Setup

The spring model presented in Section 3.1 was validated by measuring actual spring deflections for given loads. Figure IV.1 describes a simple test rig to measure the stiffness of springs. Two springs were placed between a top plate and a bottom plate. The spring pitch and overall diameter in the test were 3.2mm and 3mm, respectively, rendering a slightly stiffer support than actual springs (pitch 3.55mm, diameter of 2.9mm) used in the foil gas bearing with compression springs. As seen in the Figure IV.1, the top and bottom plates have guide rails with small clearances that allow the springs to stretch in the axial direction. In addition, the bottom plate has a through-hole in the middle of the plate to connect the top plate and a static loader with a cable. The static loader, located under the test rig base, is a simple container that holds known weights. Both the top and bottom plates used a bare stainless steel pair and a Teflon-coated steel pair to simulate a near-pinned case and a near-free sliding case, respectively.

Vertical loads from 0.23 to 1.68N were applied to the top plate from the static loader and a total of 20 spring deflections were measured for each load. After each loading cycle, the test springs were completely relaxed from any hysterisis by gently tapping the top plate. An eddy current proximity probe, installed vertically against the top plate, measured the displacements, and a 5360 BK precision 4 digit digital multimeter displayed the voltage signals from the sensor. See Table IV.1 for the detailed test conditions.

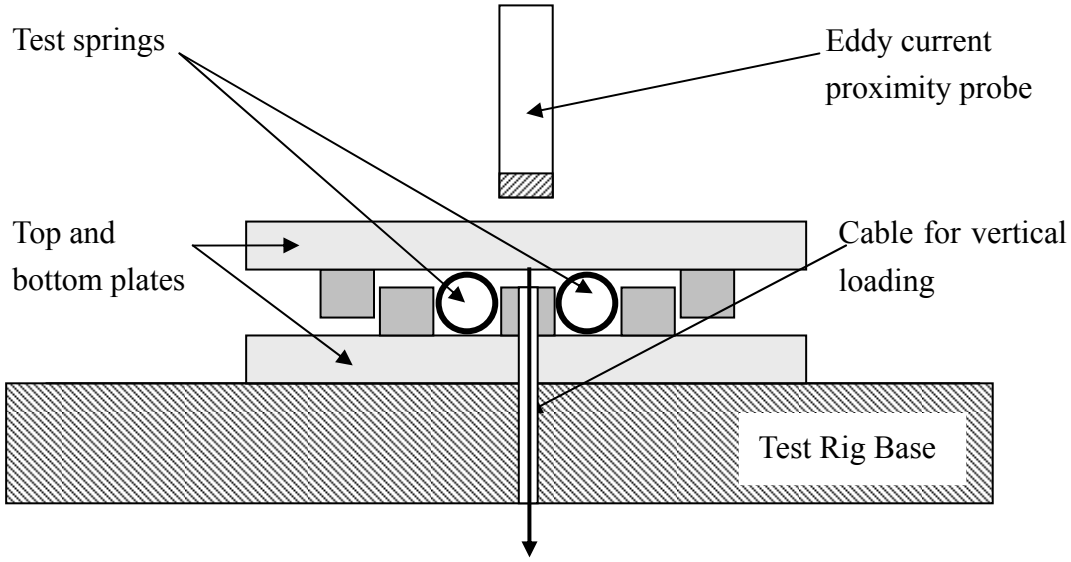


(a) Schematic view of a test rig to measure spring bump stiffness

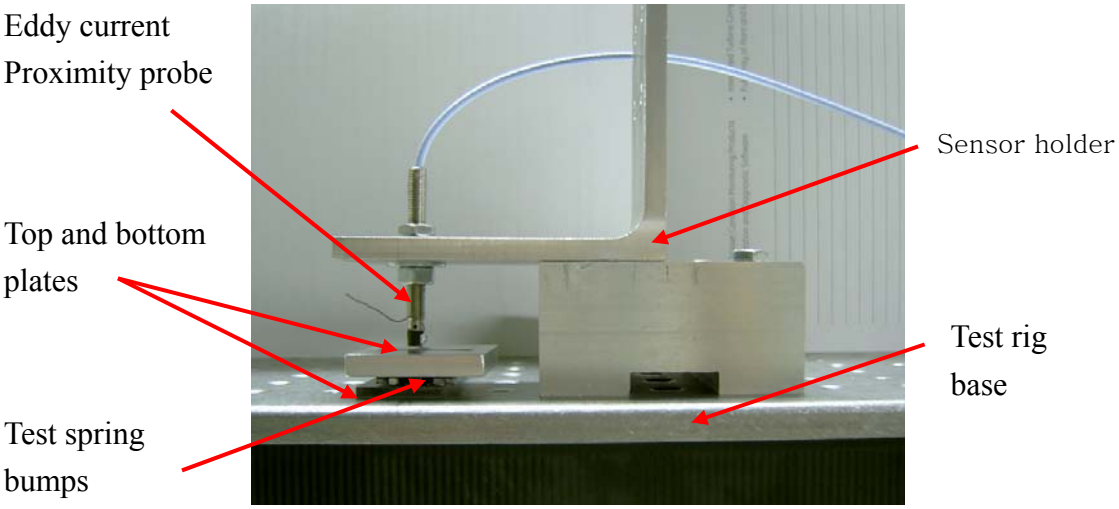


(b) Photo of a test rig to measure spring bump stiffness

**Figure IV.1 Test rig to measure spring stiffness**

**Table IV.1 Test conditions for spring stiffness measurements**

| Measurement Conditions | Measurement Values |
|---|---|
| Eddy current sensor sensitivity | 87.40 μm/V |
| Spring dimension (length/diameter/pitch) | 32.00/3.00/3.2 mm |
| Number of test springs | 2 sets ( 4 each ) |
| Applied static loads | 0.23, 0.47, 0.70, 0.94, 1.18, 1.43, 1.68 N |

### 4.1.2 Experimental Results

Figure IV.2 shows the measured load-deflection curves being overlapped with predictions (demonstrated by the dotted straight lines). The spring simulation model predicted constant stiffness regardless of load because a small deflection (with a constant overall spring diameter and pitch) was assumed. Measured stiffness was at 95% confidence intervals from the 20 measurements taken for each load. The measured stiffness for the near-pinned case was slightly larger than the prediction at the small loads level, and exhibits a hardening effect as the applied load increased, showing a non-linear behavior. For the near free-free case with Teflon coated surfaces, the measured stiffness at low loads showed a very good level of agreement with the predictions.

Even if the measured stiffness with stainless steel surfaces is a little higher than in the pinned case, fine scratch marks on the test surfaces evidence the presence of a microscopic slip (dry friction damping) of the springs. This phenomenon can be expected because the spring model assumes that the friction forces are conservative forces applied in the opposite direction to the spring sliding. This assumption, for the case of high friction, predicts the inward contraction of springs (in the same direction as the friction). It contradicts to the actual physical phenomena; the spring undergoes outward stretching even under high friction if an elastic pushing force is lager than the friction. For conventional bump foil bearings, bump pitch is much larger than bump height. Therefore, other simulation models [6, 21] similar to that in this research (using friction forces as conservative forces) predict sliding opposite to the friction force, mimicking actual physical phenomena up to marginally high friction coefficients.

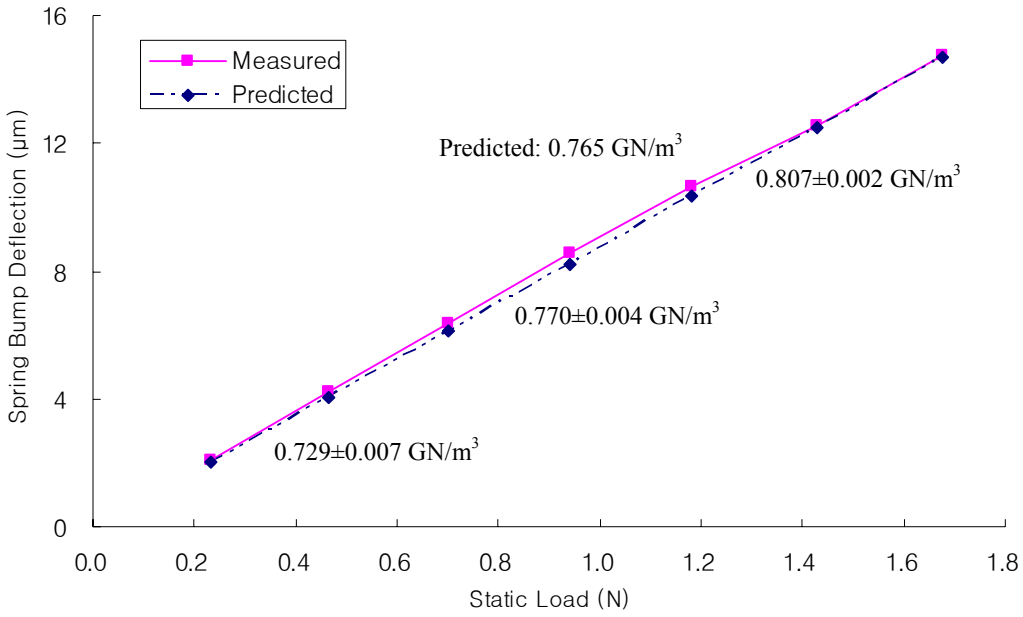


(a) Spring deflection test for free-free condition

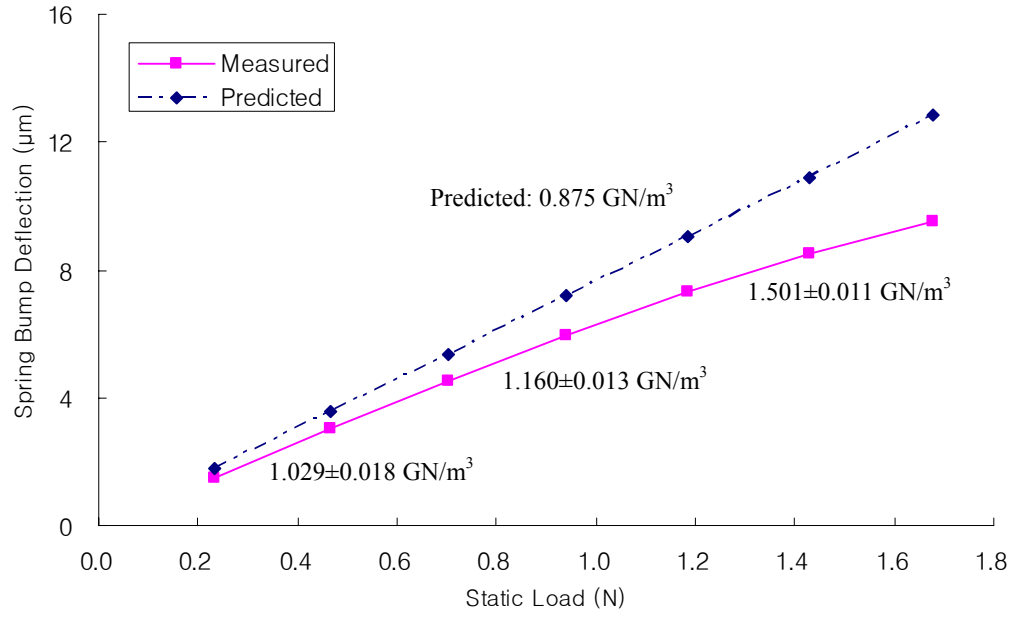


(b) Spring deflection test for pinned condition

**Figure IV.2 Measured and predicted deflections of test springs with load (Numbers represent predicted and measured spring stiffness)**

**Table IV.2 Experimental results of spring stiffness measurements**

| Applied Static load (N) | Measured Deflection (μm) | Measured $k$ (GN/m$^3$) | Uncertainty with 95% Confidence | Predicted $k$ (GN/m$^3$) |
|---|---|---|---|---|
| 0 | 0 | - | - | - |
| 0.232 | 2.102 | 0.709 | 0.007 | 0.765 |
| 0.466 | 4.239 | 0.729 | 0.007 | 0.765 |
| 0.703 | 6.380 | 0.749 | 0.003 | 0.765 |
| 0.941 | 8.556 | 0.770 | 0.004 | 0.765 |
| 1.183 | 10.637 | 0.789 | 0.003 | 0.765 |
| 1.428 | 12.577 | 0.807 | 0.002 | 0.765 |
| 1.678 | 14.736 | 0.828 | 0.003 | 0.765 |

(a) Deflection and stiffness of test springs for free-free condition

| Applied Static load (N) | Measured Deflection (μm) | Measured $k$ (GN/m$^3$) | Uncertainty with 95% Confidence | Predicted $k$ (GN/m$^3$) |
|---|---|---|---|---|
| 0 | 0 | - | - | - |
| 0.232 | 1.490 | 1.069 | 0.014 | 0.875 |
| 0.466 | 3.035 | 1.029 | 0.018 | 0.875 |
| 0.703 | 4.527 | 1.062 | 0.018 | 0.875 |
| 0.941 | 5.941 | 1.160 | 0.013 | 0.875 |
| 1.183 | 7.300 | 1.314 | 0.013 | 0.875 |
| 1.428 | 8.508 | 1.501 | 0.011 | 0.875 |
| 1.678 | 9.520 | 1.693 | 0.012 | 0.875 |

(b) Deflection and stiffness of test springs for pinned condition

## 4.2 Load Capacity Measurements

### 4.2.1 Experimental Setup

The Load capacities of the test foil gas bearing were measured at 20,000 rpm both with and without cooling. Figure IV.3 shows a photo of the load capacity test rig. A precision-grounded rotor was supported by two ball bearings and connected to a DC motor via a flexible coupling. The test foil gas bearing was assembled on to the shaft with its housing connected to a tension cable under static loads, which are in upward direction. Three air jet nozzles supplied cooling air to the ball bearings to maintain a steady temperature on the rotor surface when the test bearing was not loaded. Two thermo couples (located at the center and 0.15 inches from the edge) attached on the backside of the top foil measured the bearing temperatures at the loaded zone. The nominal bearing clearance was estimated to be 47 μm from precise measurements of the rotor and the constituent components of the bearing. Table A.1 shows a detailed test rig component specification.

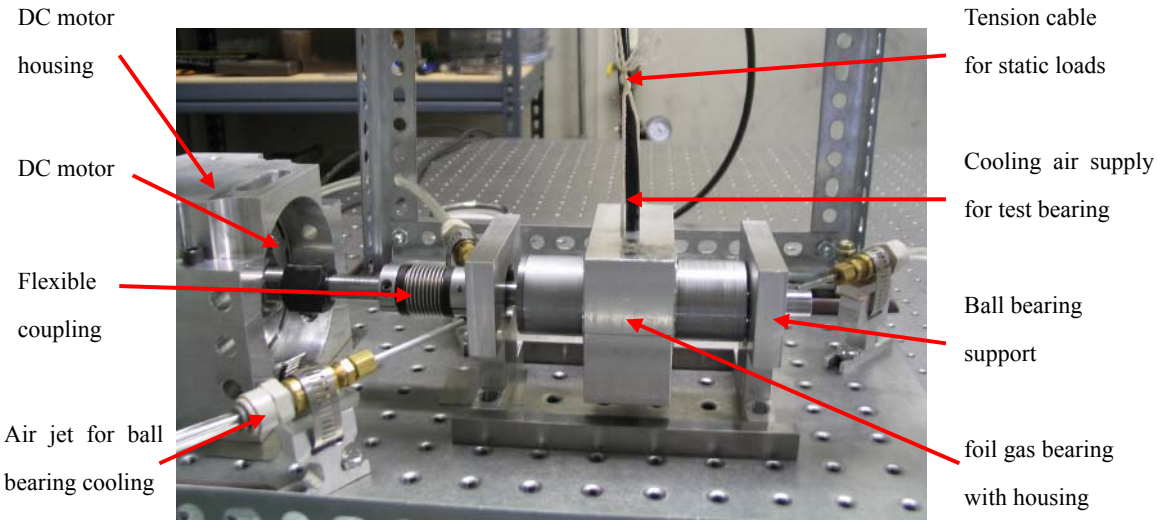


**Figure IV.3 Load capacity measurement test rig**

Cooling air to the bearing was supplied through a single 1/4 inch tube as seen in Figure IV.3. The supplied air was distributed through the cooling jacket formed on the bearing housing to the three plenum chambers (see Figure IV.4 b). Three sets of two air supply holes (for a total of six holes) were machined 120° apart on the bearing sleeve along the circumferential direction (as seen in Figure IV.4) and the cooling air from the three plenum chambers was fed through the six air supply holes on the bearing sleeve to the backside of the top foil. Because the springs are not connected in the circumferential direction (see Figure II.2), the cooling air supplied through these holes was expected to cool a wide surface of the top foil.

Thermocouples were connected to an Omega DP 472-T-C2 6 channel temperature display and measured signals were sent to an RS-232 data acquisition program for recording. Static loads ranging 15.9N to 108.6N were applied directly to the test foil gas bearing through a string from the static loader. Detailed test conditions are described in Table IV.3.

**Table IV.3 Test conditions for load capacity measurements**

| **Test parameters** | **Values** |
|---|---|
| Operating speed | 20,000 RPM |
| Cooling airflow | 0.085 $m^3$/minute ( 3 CFM ) |
| Applied loads | 15.9, 45.4, 65.8, 76.8, 86.8, 96.3, 108.6N |

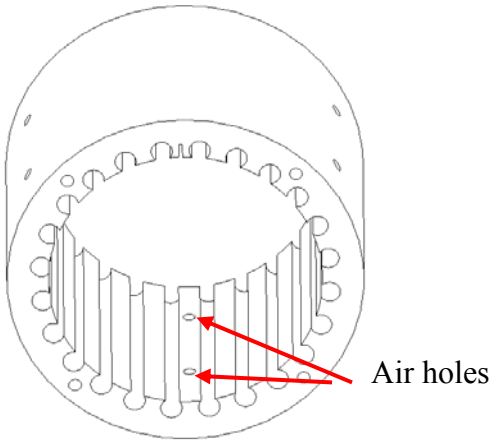


(a) Holes for cooling air on the bearing sleeve

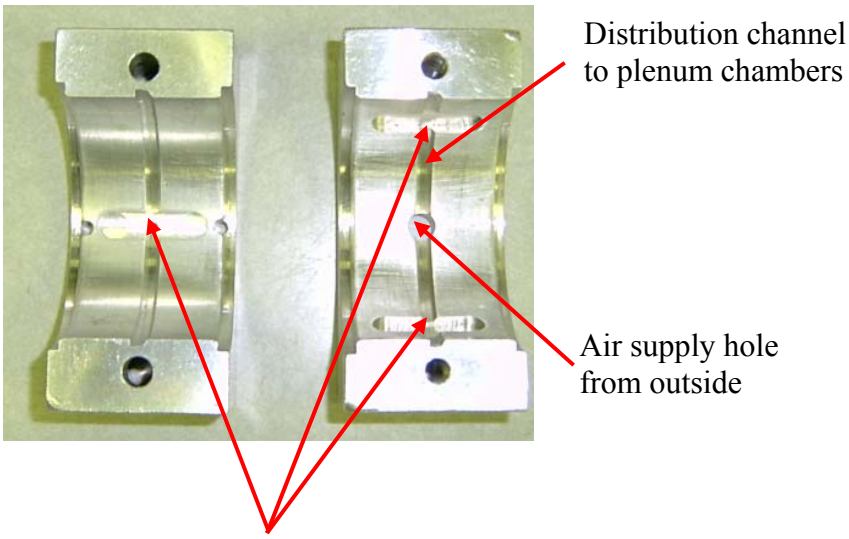


(b) Photo of cooling jacket

**Figure IV.4 Bearing cooling method: Split bearing housing with cooling jacket, surrounding bearing sleeve**

### 4.2.2 Experimental Results

Figure IV.5 (a) shows the temperature variation of an un-cooled bearing. The bearing temperature was stable at each load until 96.3N, and it began to fluctuate with the highest temperature of above 100°C upon applying 108.6N. Therefore, the load capacity of the un-cooled bearing was regard as 96.3 N (21.65 lb), 84.3kPa (12.2 psi) at 20,000 rpm. This is a similar value with the first generation bump foil gas bearing [10]. The total temperature rise up to the load capacity was about 45°C. As seen in Figure IV.6 (a), the mean temperature of the test foil gas bearing is rather steady increased with applied loads.

Figure IV.5 (b) shows the measured temperature versus time for the cooled bearing with an airflow rate of 3cfm. The initial steady state temperature under the smallest load of 16.5N was slightly lower than that of the un-cooled bearing because of the cooling air. Compared to the un-cooled case, the temperature curve did not show high peaks and the maximum temperature rise up to 96.3N was only 20°C, indicating the very effective cooling performance of the cooling jacket shown in Figure IV.4. Even if the maximum bearing temperature was below 50°C, no additional load was attempted in an effort to avoid an excessive deflection of the springs. Considering that the load capacity of the foil gas bearings is decided mainly from the structural integrity of the underlying structure if there is an effective cooling method, a usage of stiffer springs to the bearing with the suggested cooling method is expected to lead a higher load capacity.

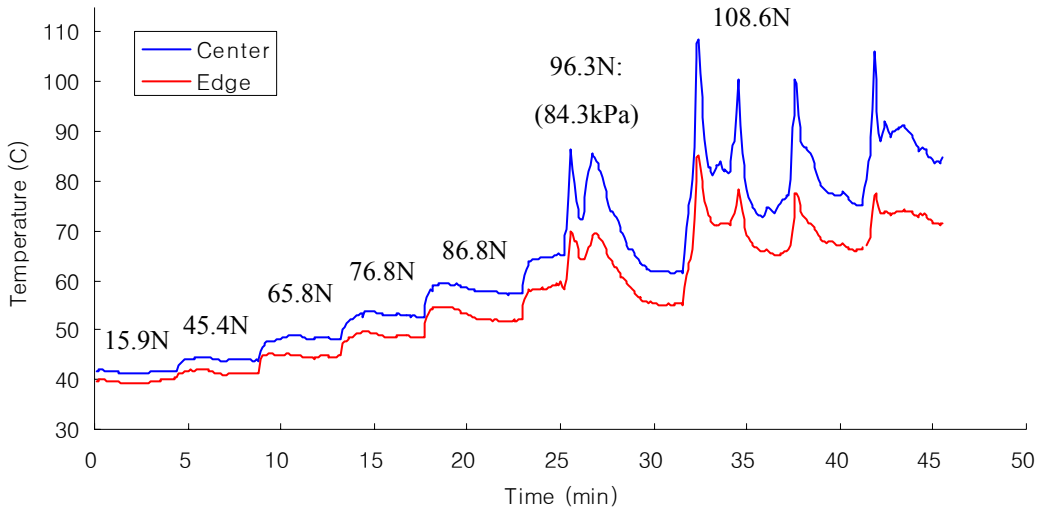


(a) Foil gas bearing temperature with load (without cooling)

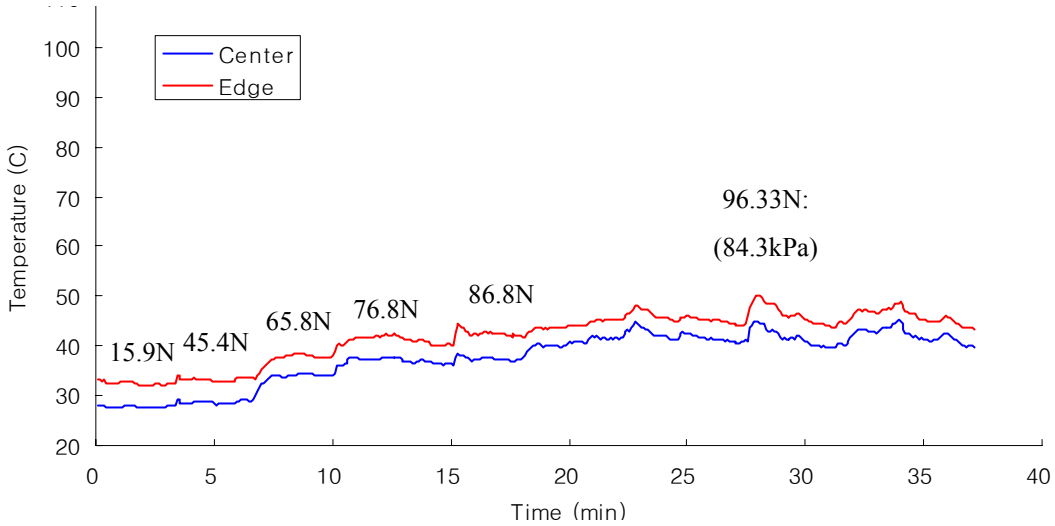


(b) Foil gas bearing temperature with load
(With cooling air flow rate of 3 cfm)

**Figure IV.5 Bearing temperature with load at 20,000rpm (both with and without cooling, numbers represent applied loads)**

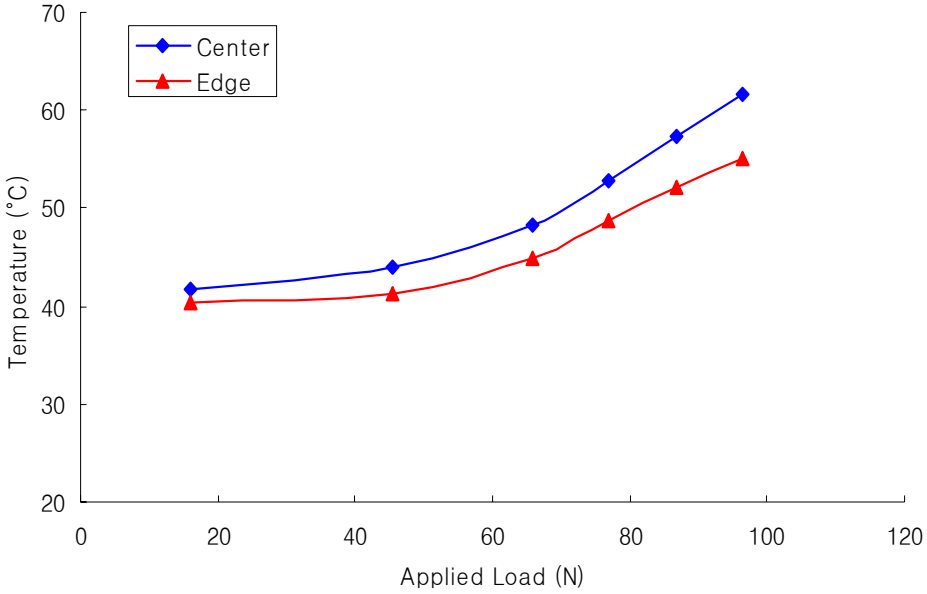


(a) Foil gas bearing temperature with load (without cooling)

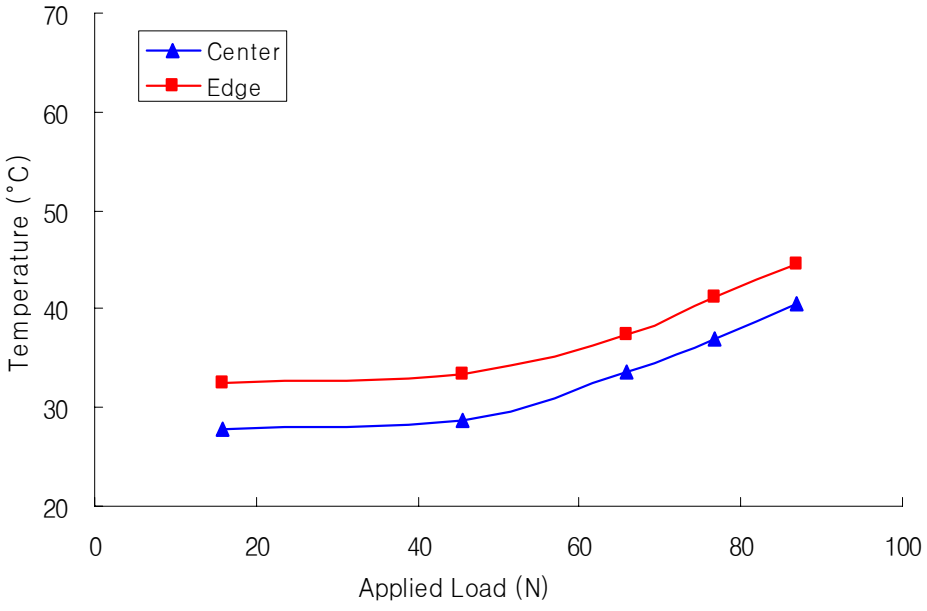


(b) Foil gas bearing temperature with load
(With cooling air flow rate of 3scfm)

**Figure IV.6 Average bearing temperature with load (both with and without cooling)**

### 4.3 Static Structural Stiffness Measurements

#### 4.3.1 Experimental Setup

The static structural stiffness of the test foil gas bearing was estimated by measuring spring deflections with a test rig in Figure IV.7. The stationary shaft was held firmly using a three-jaw chuck and a live center of a lathe to provide very stiff support. The shaft is 1.502 inches in diameter and 8 inches long with a 5 μm CrN coating (see Figure A.4 for the rotor drawing). As seen in Figure IV.7, the test bearing was assembled on the shaft with almost zero clearance. A manual dynamometer was attached to the lathe tool holder and moved horizontally to apply static loads to the bearing by rotating the lathe tool's positioning knobs. An eddy current proximity probe measured the horizontal displacement of the bearing housing (i.e. the deflection of the spring) and the BK precision digital multimeter displayed the voltage output signals.

Static loads were slowly applied to the bearing form 0 to 22N in 2N increments and then removed with in 2N decrements.

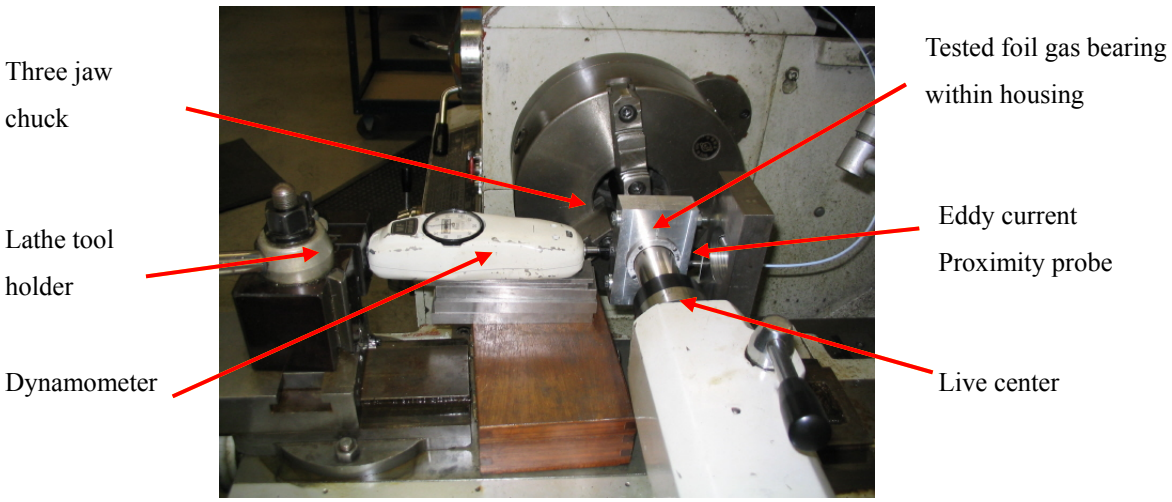


**Figure IV.7 Static structural stiffness measurement test rig**

### 4.3.2 Experimental Results

The structural stiffness of the test foil gas bearing was identified from measured displacements of the test bearing. Table IV.4 shows the average deflection and stiffness for the loading and unloading cases with a 90% confidence from five measurements. The structural stiffness of the test foil gas bearing can be evaluated by calculating the slope of the curve-fitted graph at each point, i.e., $K = \partial F / \partial x$ .

Figure IV.8 shows the average load-deflection curves and the estimated stiffness for loading cases from five tests. Hysteresis on the load-deflection curve evidences the existence of Coulomb damping in the springs.

The structural stiffness of the foil gas bearing was calculated from the slope of the load-deflection curve at each load. The uncertainty of the measured stiffness is $\pm$ $0.12\times10^5$ N/m, calculated from five measurements using student t-distribution. The structural deflection curves of the test foil gas bearing show a highly nonlinear behavior similar to the bump foil bearings reported in [22].

As seen in Figure IV.8 (b), the static structural stiffness of very small loads under 5N was measured to be about 38% smaller than the free-free case under the assumption of 100% contact of all the springs. This implies that geometrical uncertainty, such as precision errors of constituent components of the bearing and rotor have rendered contacts of the stationary shaft with only a few springs through the top foil. However, when the applied loads were between 5 and 10N, the measured structural stiffnesses were in the range of the free-free case ($7.06\times10^5$ N/m) and pinned case ($8.21\times10^5$ N/m) assuming that all the springs make contacts with top foil (under zero bearing clearance). Higher loads beyond 10N produced a higher stiffness than in the pinned case, indicating stiffening effect of the springs by nonlinear deflections.

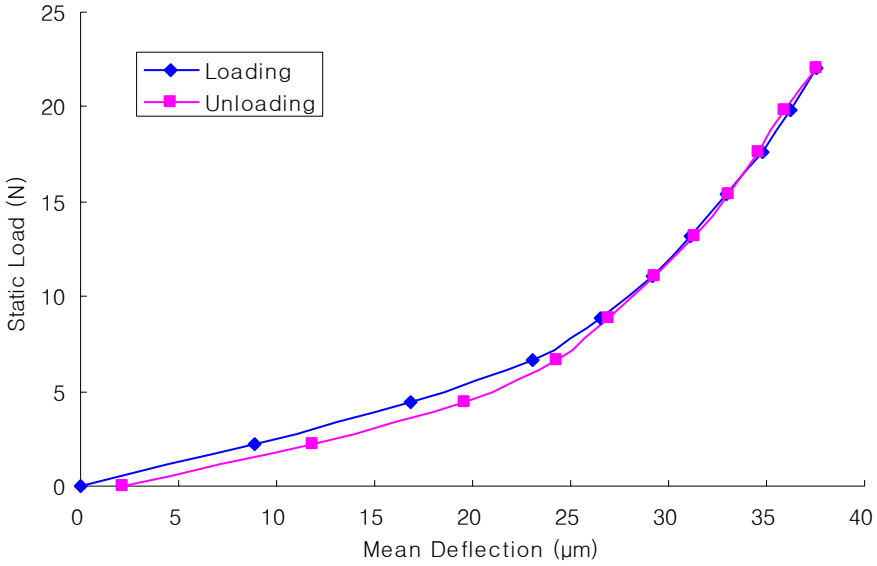


(a) Static load versus mean deflection of test foil gas bearing

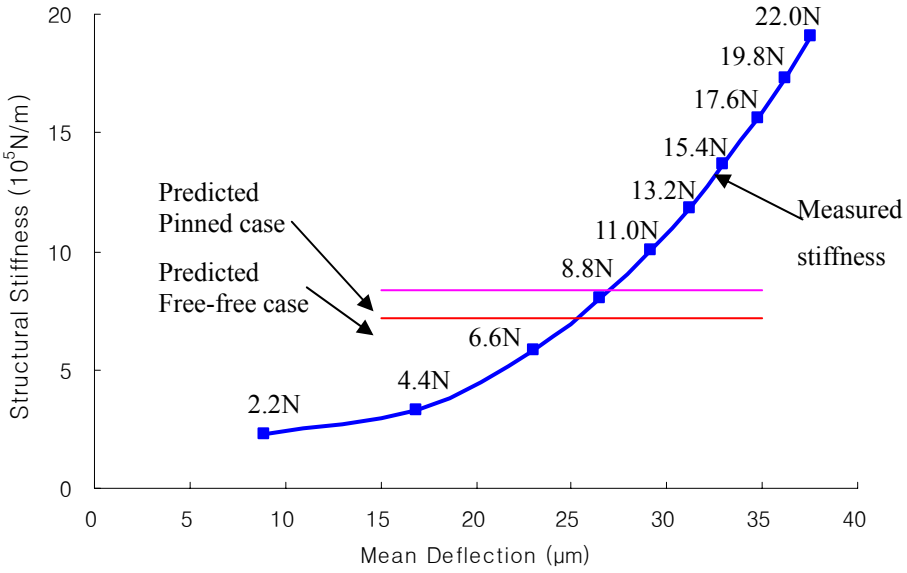


(b) Structural stiffness versus mean deflection of test foil gas bearing during loading (Numbers represent applied loads, horizontal lines are for predicted stiffnesses assuming all the springs make contact with top foil)

**Figure IV.8 Static load and structural stiffness versus deflection**

**Table IV.4 Experimental results of structural stiffness measurements**

| Applied Static load (N) | Deflection for Loading (μm) | Uncertainty with 90% Confidence | *K* for Loading ($\times 10^5$ N/m) | Uncertainty with 90% Confidence |
|---|---|---|---|---|
| 0 | 0 | - | - | - |
| 2.205 | 8.89 | 1.78 | 2.25 | 0.364 |
| 4.410 | 16.9 | 2.68 | 3.22 | 0.334 |
| 6.615 | 23.0 | 2.67 | 5.69 | 0.678 |
| 8.820 | 26.5 | 2.67 | 7.86 | 1.089 |
| 11.025 | 29.2 | 2.64 | 9.86 | 1.186 |
| 13.230 | 31.2 | 2.77 | 11.59 | 1.382 |
| 15.435 | 33.0 | 2.70 | 13.39 | 1.501 |
| 17.640 | 34.8 | 2.73 | 15.33 | 1.597 |
| 19.845 | 36.2 | 2.80 | 16.98 | 1.802 |
| 22.050 | 37.5 | 2.86 | 18.69 | 1.906 |

(a) Structural Defection and Stiffness during loading

| Applied Static load (N) | Deflection for Unloading (μm) | Uncertainty with 90% Confidence (μm) | *K* for Unloading ($\times 10^5$ N/m)) | Uncertainty with 90% Confidence (μm) |
|---|---|---|---|---|
| 0 | 2.13 | 0.82 | - | - |
| 2.205 | 11.8 | 2.08 | 1.90 | 0.471 |
| 4.410 | 19.6 | 2.60 | 5.08 | 0.850 |
| 6.615 | 24.2 | 2.05 | 8.62 | 1.130 |
| 8.820 | 27.0 | 2.28 | 11.2 | 1.300 |
| 11.025 | 29.3 | 2.46 | 13.6 | 1.356 |
| 13.230 | 31.4 | 2.54 | 15.8 | 1.405 |
| 15.435 | 33.0 | 2.57 | 17.7 | 1.675 |
| 17.640 | 34.6 | 2.62 | 19.6 | 1.808 |
| 19.845 | 36.0 | 2.70 | 21.2 | 1.836 |
| 22.050 | 37.5 | 2.86 | 23.2 | 1.883 |

(b) Structural Defection and Stiffness during unloading

## 4.4 Dynamic Structural Stiffness and Damping Measurements

### 4.4.1 Experimental Setup

The dynamic structural stiffness and damping coefficients were measured with an existing test rig used in [16]. As seen in Figure IV.9, a stationary shaft was held firmly by an index head of an end mill to provide very rigid support. The test foil gas bearing was assembled with almost zero clearance (estimated from measurements of the constituent parts) to minimize any secondary dynamics involved with the top foil and the springs. The test foil gas bearing was connected to an electromagnetic shaker via a slender stinger. The force transducer located between the stinger and the bearing housing measured the dynamic force applied to the bearing. A piezoelectric accelerometer attached to the bearing housing measured its acceleration. An eddy current proximity probe measured the horizontal displacement of the bearing.

The test foil gas bearing was excited with the electromagnet shaker from 20 to 400Hz with 20 Hz increments. Three different magnitudes of loads, i.e., 4N, 8N, and 12N, were applied. A DC voltage offset from the proximity sensor was adjusted using a signal conditioner, and two oscilloscopes monitored the time traces of the sensors. Four signals from the force transducer, displacement, accelerometer, and frequency were connected to the data acquisition board and recorded with digital signal analyzer.

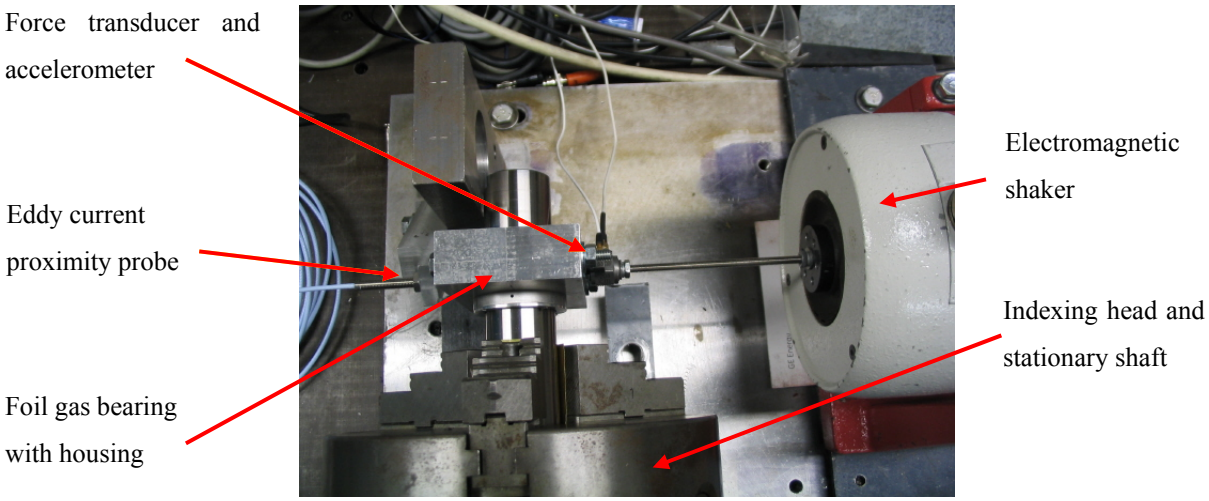


(a) Dynamic stiffness and damping test rig

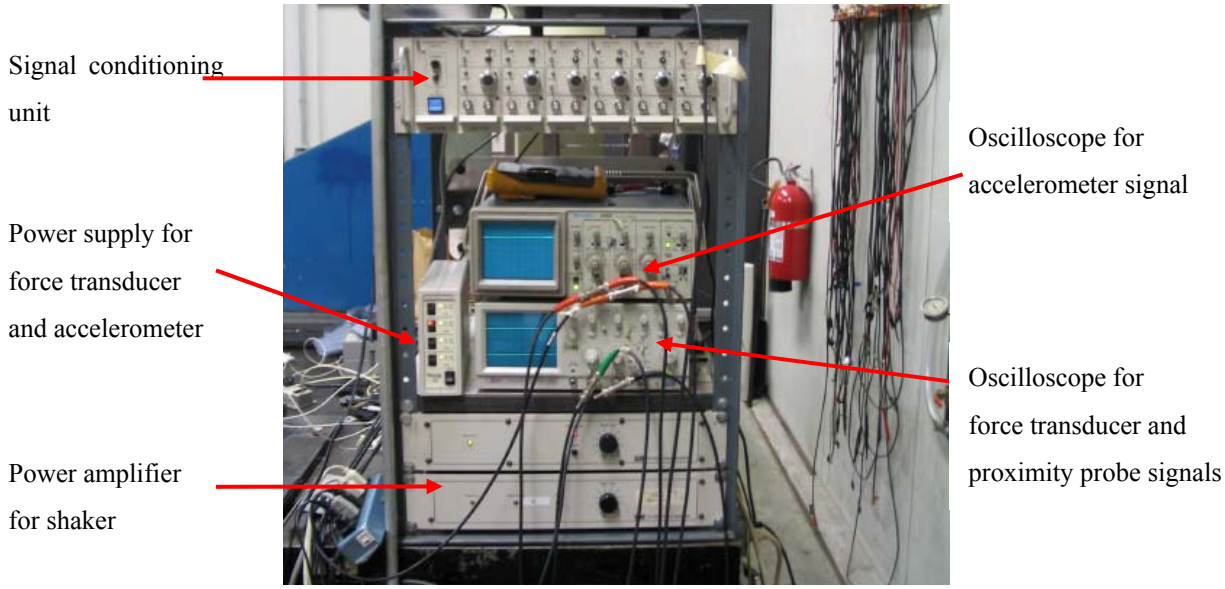


(b) Dynamic stiffness and damping measuring instruments

**Figure IV.9 Dynamic structural stiffness and damping measurement test setup [16]**

### 4.4.2 Parameter Identification of Test Foil Gas Bearing

Identifications of the dynamic structural stiffness and damping coefficients of the test foil gas bearings follow the method presented in [16]. Detail processors are reviewed as follows.

The test foil gas bearing with its housing is modeled as a single degree of freedom (SDOF) mass-spring-damper system with a dynamic excitation force, *F(t)*;

$$M_{sys}\ddot{x}(t) + C_{eq}\dot{x}(t) + Kx(t) = F(t) \tag{43}$$

where *F(t)* and *x(t)* represent the excitation force and system displacement, respectively.

Assume $x(t) = Xe^{i\omega t}$ and $F(t) = F_0 e^{i\omega t}$, then

$$\left[(K - M_{sys}\omega^2) + iC_{eq}\omega\right]Xe^{i\omega t} = F_0 e^{i\omega t} = Z(\omega)Xe^{i\omega t} \tag{44}$$

The mechanical impedance of the system can be defined as

$$Z(\omega) = \frac{F_0}{X} = (K - M_{sys}\omega^2) + iC_{eq}\omega \tag{45}$$

As seen equation (45), the mechanical impedance is composed of two parts; real and imaginary parts. The dynamic structural stiffness and system mass of the foil gas bearing are determined by the frequency domain analysis of the real part of the mechanical impedance, i.e. $K - M_{sys}\omega^2$. In the graph of real part of the impedance versus $\omega^2$, y intercept is the dynamic structural stiffness of the foil gas bearing ($K$) and the slope is the system mass, $M_{sys}$ including the bearing housing.

The test foil gas bearing has compression springs under the top foil, and when dynamic force is applied on the bearing, dry friction arises due to the relative motion of the springs and the surrounding surfaces. This Coulomb friction, unlike the viscous damping force, is constant regardless of the sliding speed and always opposite to the direction of motion.

The Coulomb damping force can be defined as $F_d = \mu_d N \,\mathrm{sgn}(\dot{x}')$, where $\mu_d$ is a dry

friction coefficient, $N$ is a normal force on the surface, and sgn(τ) is a signum fuction which satisfies the following conditions; sgn(τ) = 1 when $\tau > 0$, sgn(τ) = 0 when τ = 0, and sgn(τ) = -1 when $\tau < 0$ . The foil gas bearing with the housing can be modeled as,

$$M_{sys}\ddot{x} + F_C \operatorname{sgn}(\dot{x}) + Kx = F(t) \tag{46}$$

where $F_C$ is an equivalent Coulomb damping force in the direction of the excitation.

Calculation of equivalent viscous damping follows the principle that total dissipated energy of Coulomb damping over one cycle is the same as the dissipated energy for viscous damping. The dissipated energy over one cycle from the dry friction and viscous damping forces are

$$\Delta E_C = \oint F_C \operatorname{sgn}(\dot{x}) dx = \oint F_C \dot{x}(t) \operatorname{sgn}(\dot{x}) dt \tag{47.a}$$

$$\Delta E_V = \oint C_{eq} \dot{x} dx = \oint C_{eq} \left[\dot{x}(t)\right]^2 dt \tag{47.b}$$

,respectively. The dissipated energy should be the same as the work done by the excitation force, *F(t)*, which is given by

$$W_{sys} = \oint F(t) \dot{x}(t) dt \tag{48}$$

Therefore, the equivalent Coulomb damping force in the direction of spring deflection and the equivalent viscous damping coefficients become

$$F_C = \frac{W_{sys}}{\oint \dot{x}(t) \operatorname{sgn}(\dot{x}) dt} \tag{49.a}$$

$$C_{eq} = \frac{W_{sys}}{\oint \left[\dot{x}(t)\right]^2 dt} \tag{49.b}$$

, respectively.

### 4.4.3 Experimental Results

Figure IV.10 (a) shows real part of the impedance as a function of excitation frequency. The structural stiffness of the test foil gas bearing was estimated about 1.13~1.36 MN/m, with a decreasing tendency with dynamic load, which is a similar behavior to the bump foil bearings reported in [16]. The estimated system mass (0.50~0.55 kg) was very close to the actual mass of the bearing and its housing (0.480kg), indicating little inertia of the springs. The bearing natural frequency was estimated as 240~250Hz from the given mass. Detailed estimation results for structural stiffness and system mass are described in Table IV.5

The decreasing tendency of stiffness with the dynamic load is opposite to the case of static stiffness measurements, in which larger loads produced a larger stiffness. Another interesting thing is that the measured dynamic structural stiffness within the load ranges (4-12N) is close to the pinned case, indicating that dry friction stick-slip under sinusoidal excitation may prevent the springs from slipping very effectively, especially in the case of small loads. As presented also in [16], larger sinusoidal loads produces smaller dynamic bump structural stiffness, implying more effective bump slips. Similar tendencies can be observed in Figure IV.10 (a), even if the dynamic loads applied to the bearing are relatively small as compared to the loads used in [16]. For the static structural stiffness measurements in Figure IV.8, even a small static load of 5-10N may push the springs effectively enforcing a steady slip against the bearing sleeve without generating stick-slip behavior. Figure IV.11shows the relationship between the measured static structural stiffness and the estimated dynamic structural stiffness with applied loads of 4 and 12N.

**Table IV.5 Estimated structural stiffness and system mass**

| Applied load (N) | Structural stiffness (GN/m) | System mass (kg) |
|---|---|---|
| 4 | 1.365 | 0.553 |
| 8 | 1.249 | 0.532 |
| 12 | 1.131 | 0.502 |

(Actual system mass: 0.480kg)

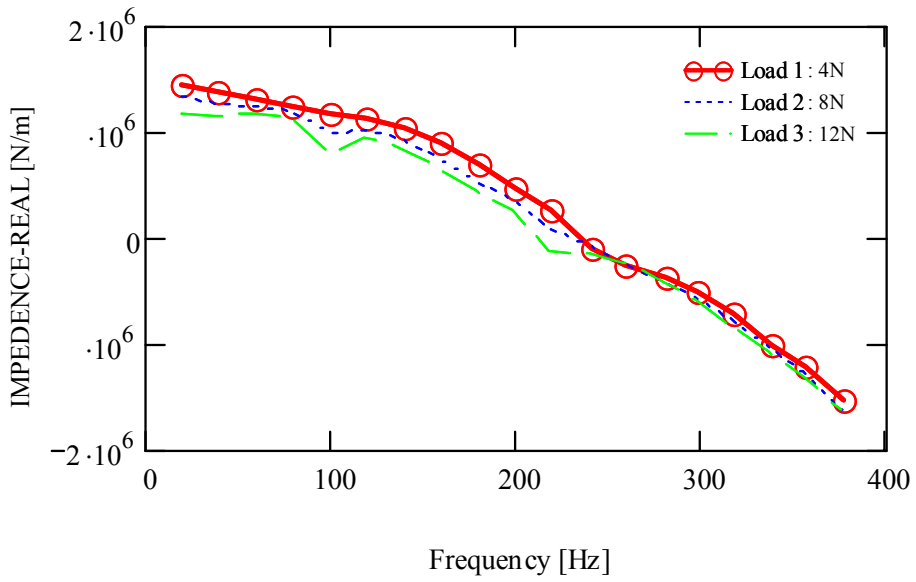


(a) Real part of test foil gas bearing system impedance

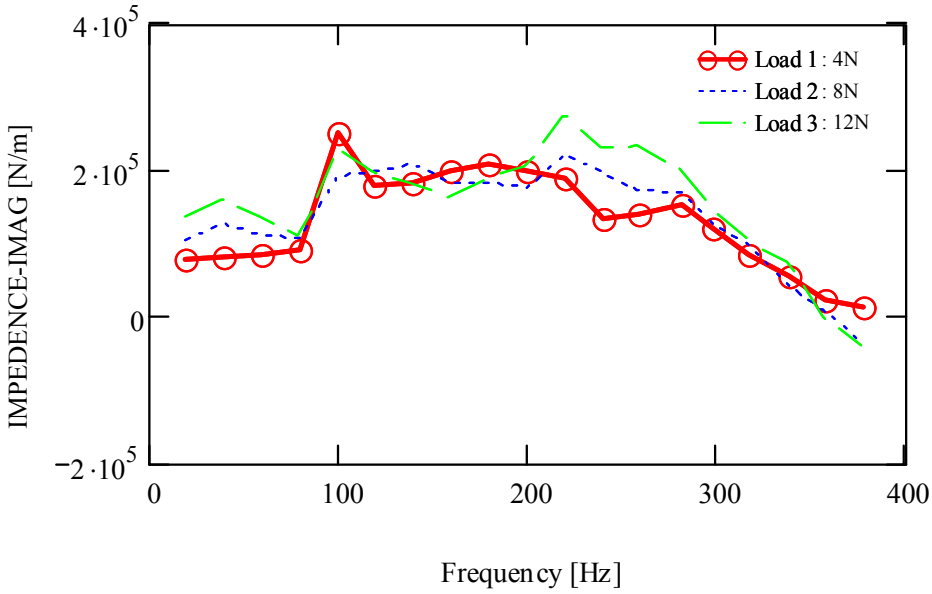


(b) Imaginary part of test foil gas bearing system impedance

**Figure IV.10 Real and imaginary part of mechanical impedance as function of excitation frequency; applied loads = 4, 8, 12N**

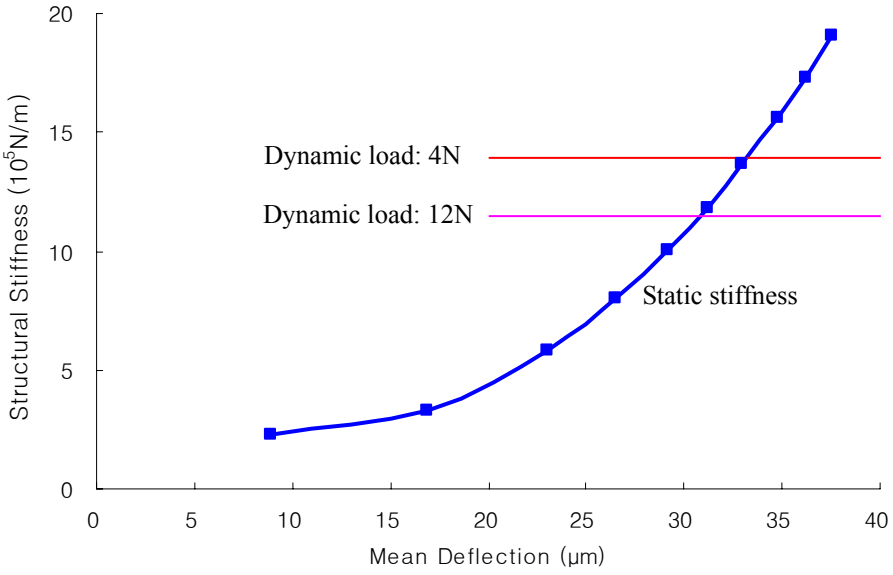


**Figure IV.11 Static and dynamic structural stiffness versus mean deflection**

The equivalent viscous damping coefficient and the structural loss factor of the foil gas bearing was evaluated from the energy dissipated over one period of motion. Figure IV.12 shows the estimated equivalent viscous damping coefficient $C_{eq}$ for three loads. In the figure, $C_{eq}$ decreases exponentially with the driving frequency and it becomes almost null above 350Hz. For the linear systems, equivalent viscous damping coefficients should be constant regardless of the amplitude of applied forces. However, measured damping coefficients increase slightly with an applied dynamic load, supporting the evidence of more effective slip under larger load amplitudes. In addition, the structural loss factor of the bearing $\gamma$ was determined with three different dynamic loads. As seen in Figure IV.13, the measured $\gamma$ increases with the dynamic load and after 250Hz, it starts to decrease and becomes to null. All the calculations were done with existing Mathcad program [23].

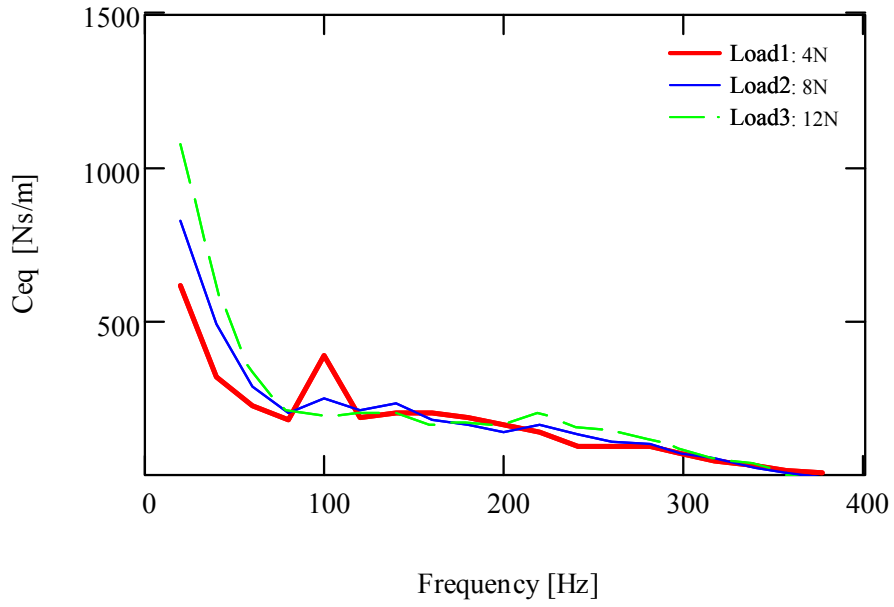


**Figure IV.12 Equivalent damping coefficient as function of excitation frequency; applied loads = 4, 8, 12N**

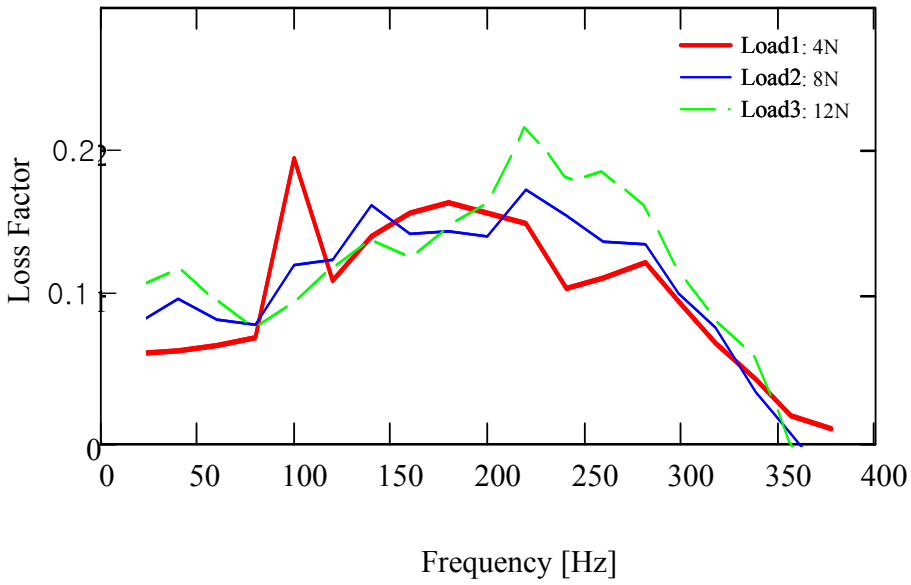


**Figure IV.13 Structural loss factor as function of excitation frequency; applied loads = 4, 8, 12N**

# CHAPTER V

# DESIGN IMPROVEMENT

The initial selection of compression springs was made without a preliminary calculation of their stiffness. Due to the soft support structure, measured stiffnesses are rather smaller than those of conventional bump foil gas bearings. A series of parametric design studies were performed to maximize the stiffness with as large spring pitch as possible. Note that the large spring pitch is desirable for easy stretching of the springs and thus large damping. To maintain the sizes of current rotor, top foil, and bearing sleeve, the design variables for parametric studies were restricted to the wire diameter and pitch, maintaining a consistent overall diameter and axial length in the springs.

## 5.1 Effect of Wire Diameters on Stiffness of Compression Springs

To investigate the effect of wire diameters on the stiffness of compression springs, the stiffness of the spring was measured with various wire diameters of two different numbers of coils (windings), i.e., 6 and 9. In the spring, the number of coils determines the spring pitch, i.e. pitch = total spring length /number of coils.

Figure V.1 shows the relation between the wire diameter and the spring stiffness for 6 coils and 9 coils. The wire diameter of the compression springs changes from 0.254mm (0.010 inch) to 0.559mm (0.022 inch) with 0.051mm (0.02 inch) increment. The chosen wire diameters are from product specification. As seen in the Figure V.1, the spring stiffness increases proportionally to the $4^{th}$ power of the wire diameter for both 6 and 9 coils.

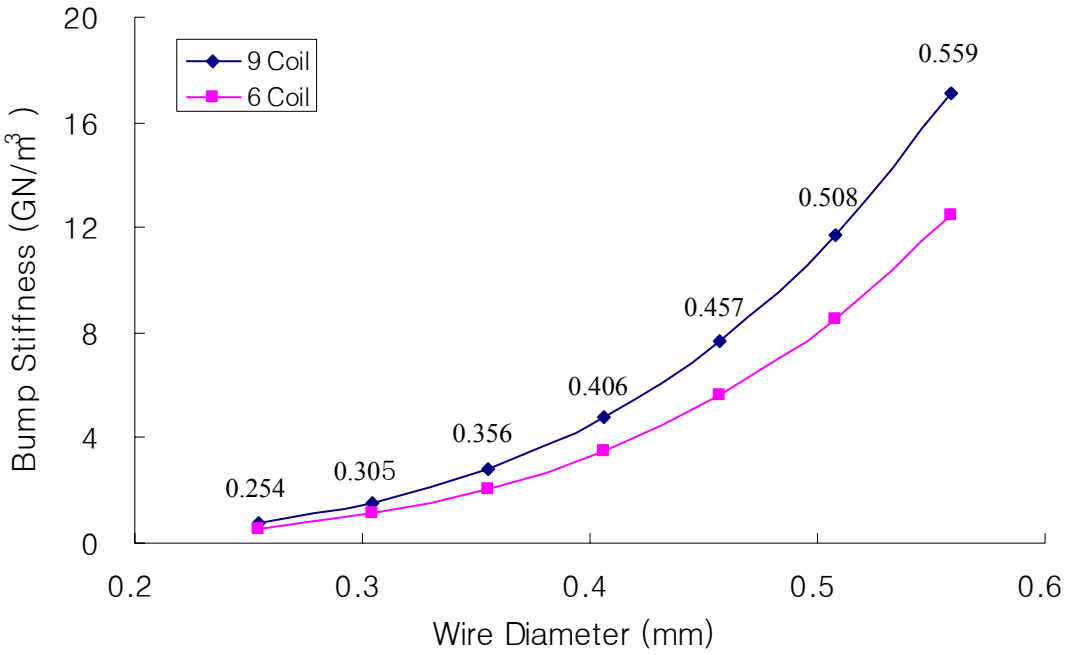


**Figure V.1 Spring stiffness versus wire diameter; numbers on graph are wire diameters**

### 5.2 Effect of Spring Stiffness on Stability of Rotor-Bearing System

Rotor-bearing orbit simulations with various spring stiffnesses were performed to investigate the effect of the stiffness on the instability. The compression spring with a wire diameter of 0.254mm and 9 coils were used for these orbit simulations. For all the parametric studies, the rotor mass and the bearing clearance are 0.6kg and 25μm, respectively. Figure V.2 shows that there is a range for the spring stiffness. Initially the onset speed of instability increases with the spring stiffness, but decreases above 5 $GN/m^3$. Above the $5GN/m^3$, the foil gas bearings behave like plain journal gas bearings, rendering a lower onset speed of instability.

As seen in Figure V.2, the optimum value for the spring stiffness is about 4.5 ~ 5.5 $GN/m^3$. A compression spring with a wire diameter of 0.406mm and 9 coils gives the stiffness of 4.8 $GN/m^3$ and a compression spring with a wire diameter of 0.457mm and 6 coils gives the stiffness of 5.6 $GN/m^3$.

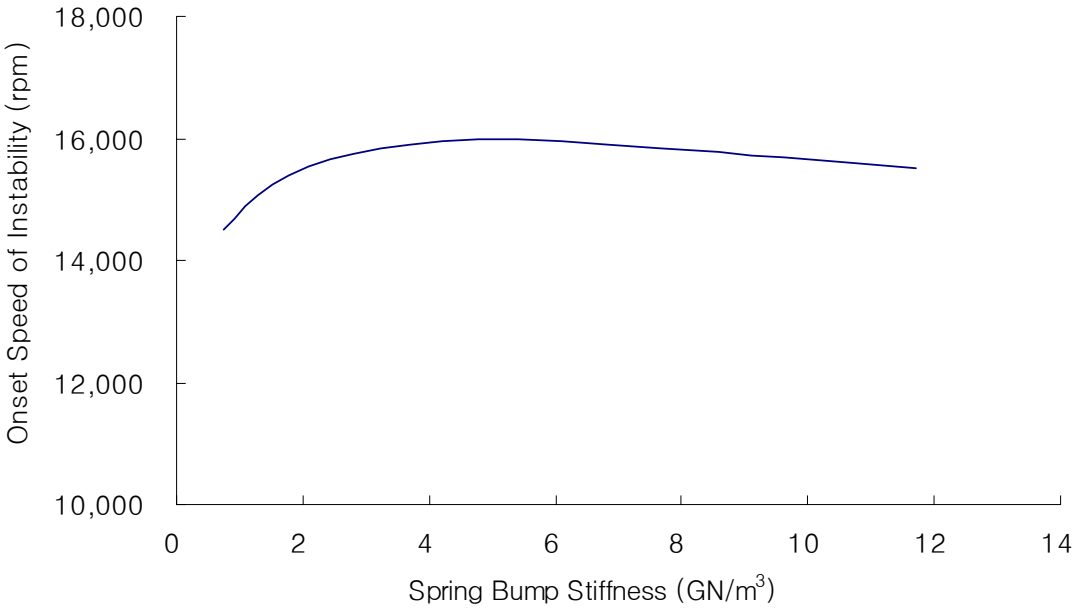


**Figure V.2 Onset speed of instability versus spring stiffness**

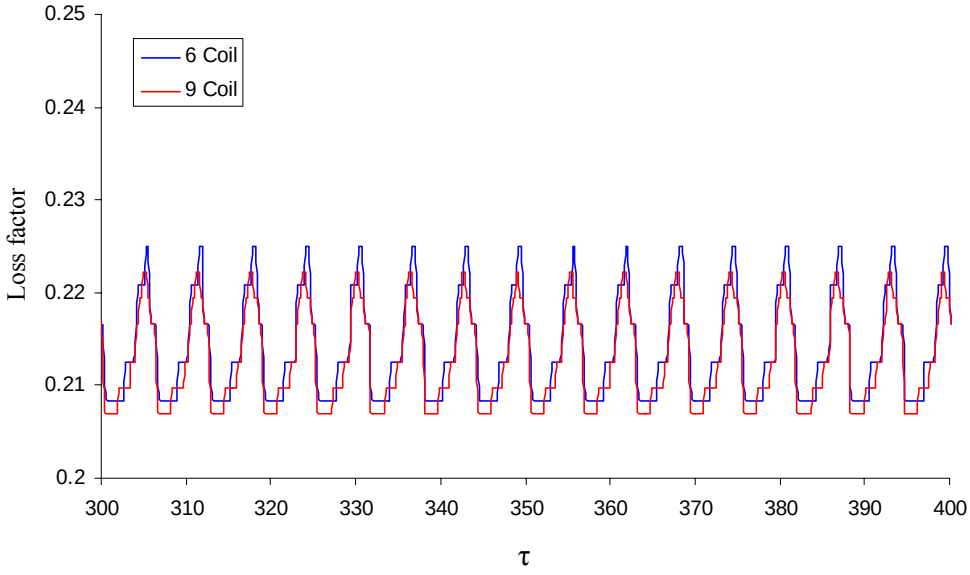


**Figure V.3 Loss factor of compression springs with 6 and 9 number of coils**

Figure V.3 shows cyclic variations of loss factors at 14,000 rpm for the two springs.

The bearing with compression springs of 6 coils has slightly higher loss factor, due to the larger pitch. However, the difference is very small, and practically it can be assumed that they would show very similar damping and rotor dynamic performance. Onset speeds of instability for the two bearings are almost identical at around 16,000 rpm.

### 5.3 Effect of Rotor Mass and External Load on Stability of Rotor-Bearing System

Hydrodynamic instability is caused by the destabilizing force in the direction of forward whirl, generated by large cross coupled stiffness. In general, the destabilizing force becomes large when the rotor eccentricity approaches zero. Therefore, it is desirable to increase the operating eccentricity for the stability of the rotor [24, 25].

Firstly, rotor mass was gradually increased to investigate the effect of increased rotor mass (i.e., load by the rotor weight itself). Two mechanisms can play in the stability when rotor mass is increased; a heavier rotor renders larger eccentricity with a penalty of increased inertia and low natural frequency. Considering the hydrodynamic instability is often observed with a whirl frequency ratio of near 0.5, the onset speed of instability also decreases as the rotor-bearing natural frequency (or approximately critical speed) decreases. On the other hands, larger eccentricity by the heavier rotor can produce larger direct damping and less cross-coupled stiffness, rendering higher stability. Figure V.4 shows onset speed of instability as a function of rotor mass for the foil bearing with spring stiffness of 5.7GN/m$^3$ (0.457mm wire with 6 coils). Interestingly enough, bearing stability is a weak function of rotor mass; the onset speed of instability increases slightly with the rotor mass.

Applying additional apparent load with small rotor mass has been the most effective way to increase gas bearing stability [25]. The old lesson could be confirmed by a series of orbit simulations using a 0.6kg rotor and increasing external loads from 6N to 30N in 6N increments. As Figure V.5 shows, the 0.6 kg rotor requires additional 30N of static load to be stable up to 45,000 rpm. Figure V.6 shows the simulated imbalance responses under static load of 30N. The hydrodynamic instability occurs at around 45,000 rpm, with a whirl speed of about 18,000 rpm, which is regarded as a natural frequency of the rotor-bearing system from the simulated amplitude and phase angle (Figure V.7) of rotor-bearing imbalance responses. As seen in Figure V.7, the critical

speed of the foil gas bearing can be estimated as 20,000rpm with a damping ratio of 0.19 (critical speed along the Y and X axes are 15,000 and 21,000 rpm, respectively).

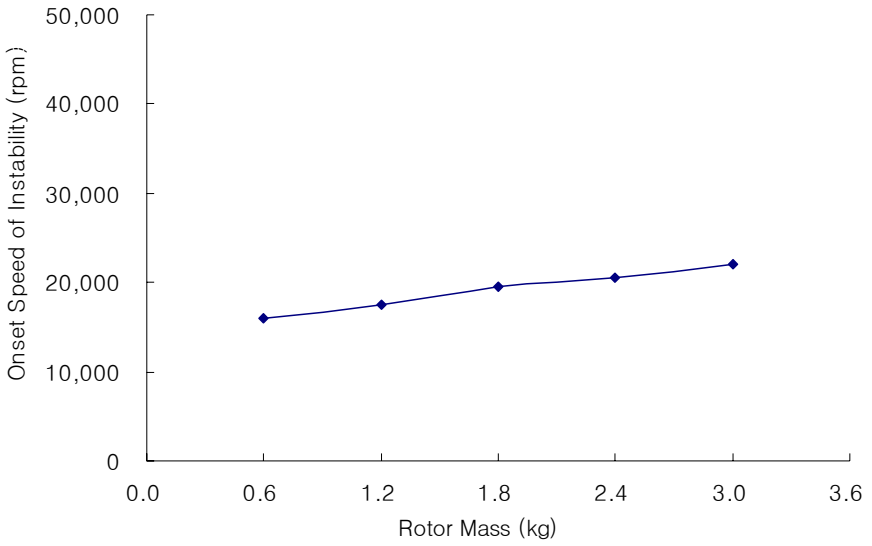


**Figure V.4 Onset speed of instability versus rotor mass; load = 0N, spring stiffness=5.7GN/m$^3$ (0.457mm wire with 6 coils)**

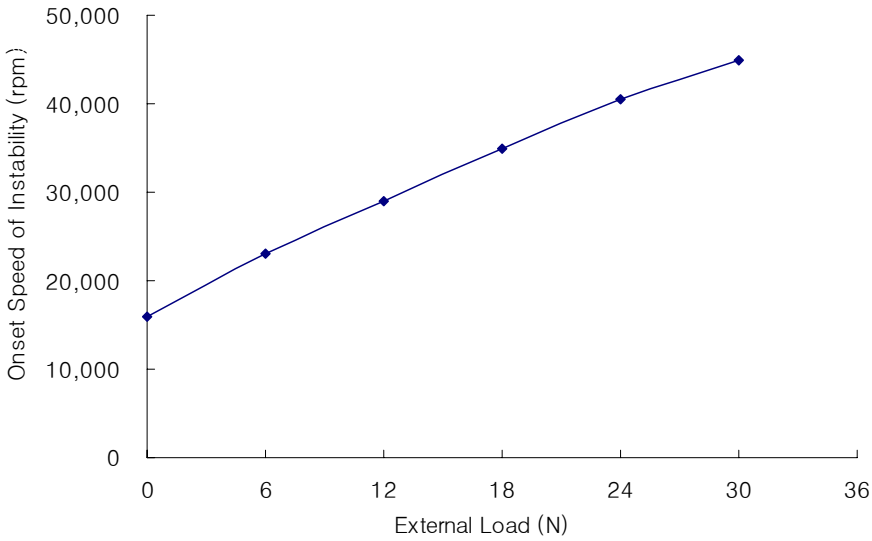


**Figure V.5 Onset speed of instability versus external load curve; rotor mass = 0.6kg, spring stiffness = 5.7GN/m$^3$ (0.457mm wire with 6 coils)**

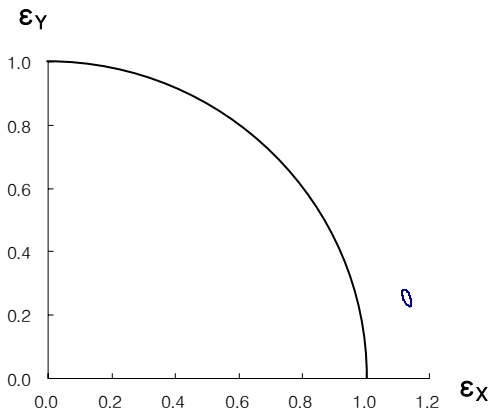


(a) 10,000 rpm

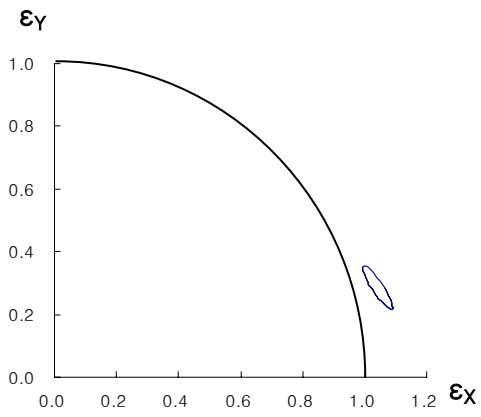


(b) 15,000 rpm

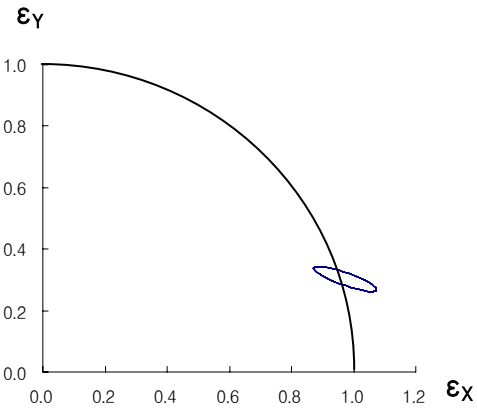


(c) 20,000 rpm

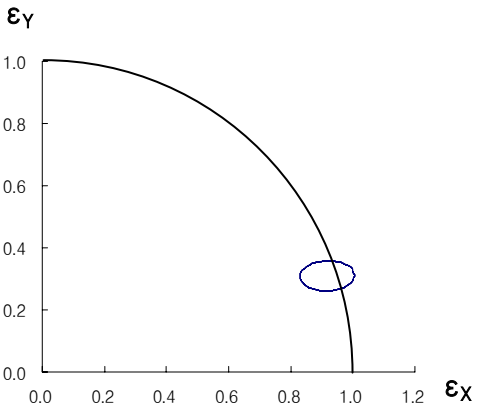


(d) 25,000 rpm

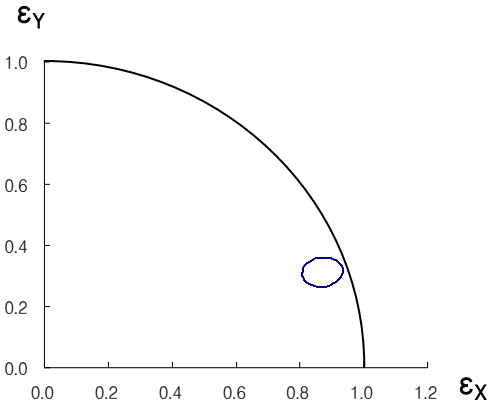


(c) 30,000 rpm

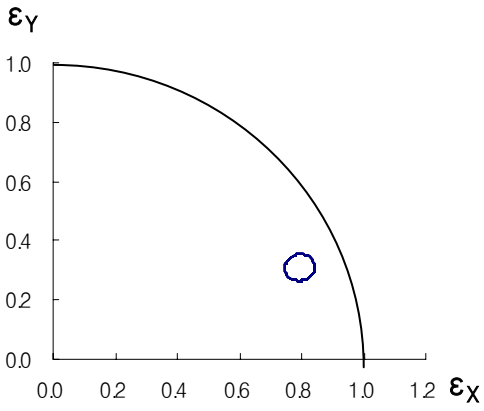


(d) 40,000 rpm

**Figure V.6 Simulated imbalance response with 30N static load in $\varepsilon_X$ direction; rotor mass = 0.6kg, spring stiffness = 5.7GN/m$^3$ (0.457mm wire with 6 coils)**

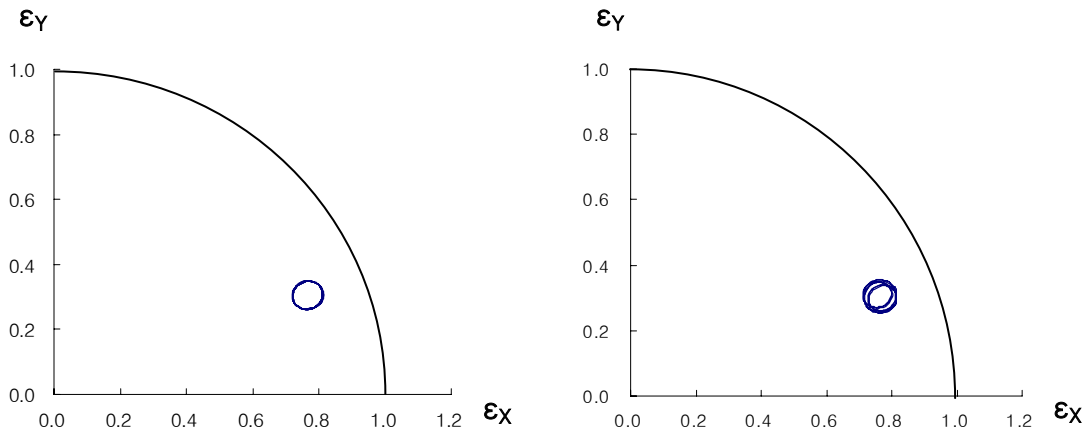


(e) 44,500 rpm (f) 45,000 rpm

**Figure V.6 Continued**

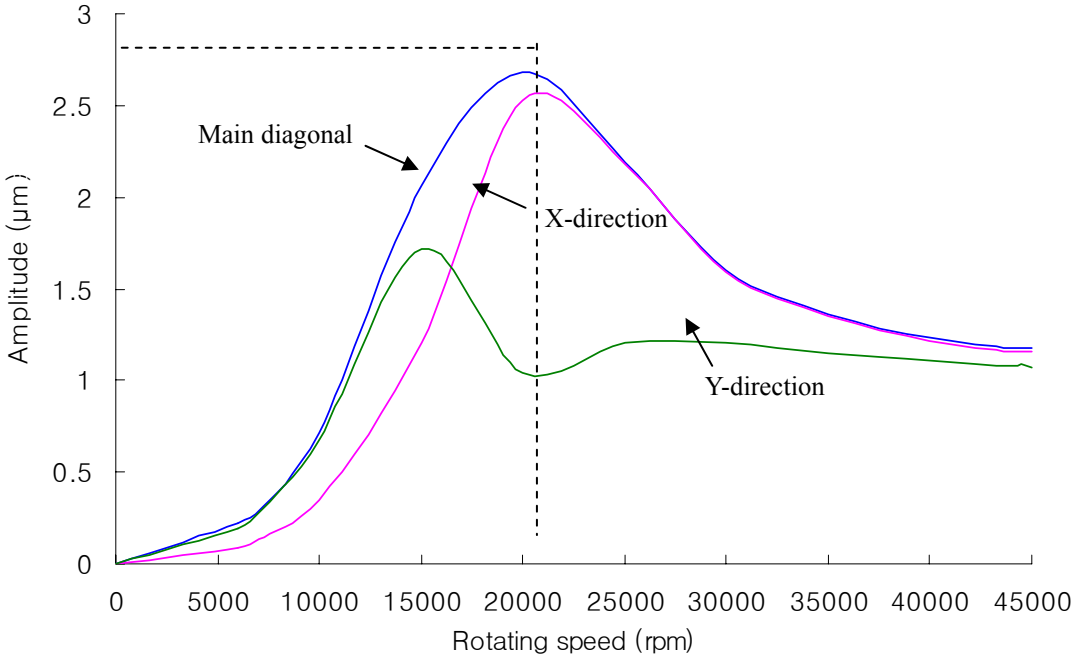


(a) Amplitudes of orbits with rotating speed

**Figure V.7 Simulated amplitude and phase angle of rotor-bearing imbalance responses with 30N static load; rotor mass = 0.6kg, spring stiffness = 5.7GN/m$^3$ (0.457mm wire with 6 coils)**

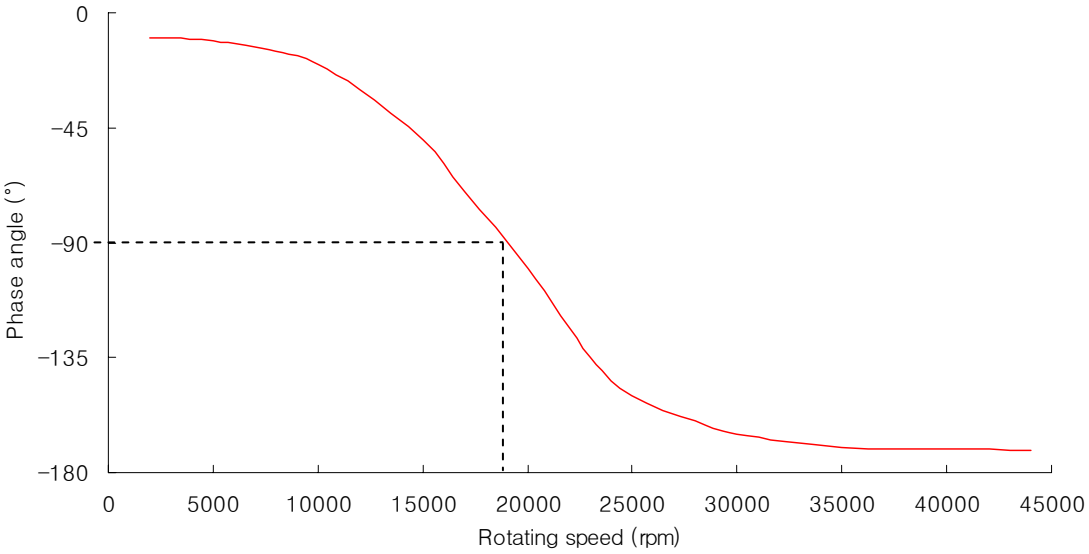


(b) Phase angle with rotating speed

**Figure V.7 Continued**

# CHAPTER VI

# CONCLUSION

The basic operating principle of bump foil bearings is the underlying compliant bump structure that provides both stiffness and damping. Foil gas bearings can be designed with any support structure providing adequate stiffness and damping to the top foil. To better understand the general behavior of foil gas bearings in a laboratory environment, a simple foil gas bearing with compression springs was designed, analyzed, and tested. This foil gas bearing used a series of compression springs as a compliant structure instead of corrugated bump foils, in order to easily change the bearing parameters. A simulation model to estimate the stiffness of a spring was developed and showed a good level of agreement with the experiments (as seen in Figure IV.2). The spring dynamics model was combined with non-linear orbit simulation to investigate the non-linear behavior of foil gas bearings. The approach can also predict structural loss factor given the geometry of the underlying springs.

Load capacity was measured to demonstrate the feasibility of the new foil bearing. A constructed bearing with rather soft springs showed a small load capacity of 96N at 20,000rpm under no air cooling. However, considering the maximum load capacity of foil bearings is determined mainly from the maximum allowable structural deflection of the underlying bump structure (under adequate cooling), increasing the structural stiffness of the test foil gas bearing using springs with larger wire diameter will increase the load capacity to the level of current bump foil bearings. A developed cooling method using direct air supply holes machined on the bearing sleeve proved to be very effective in cooling the test foil gas bearing because the springs were not connected along the circumferential direction, and therefore allowed very effective circumferential distribution of cooling air.

A measured structural stiffness and damping evidenced the existence of necessary damping for stable bearing operations. The structural stiffness of the test foil gas bearing was highly nonlinear and showed different behaviors from static loading to sinusoidal dynamic loading. For the static loading case, the structural stiffness increased with the static load (as seen in Figure IV.8), but for the dynamic loading case, the structural stiffness decreased with applied loads (as seen in Figure IV.10). This shows that under small sinusoidal loadings, presumable stick slip at the interface between the springs and

the bearing sleeve renders rather high spring stiffness close to the pinned case. The equivalent viscous damping coefficients of the test foil gas bearing was calculated from the dissipated friction energy over one excitation cycle, and the damping coefficients showed a decreasing tendency with an exciting frequency and increased with applied load amplitudes.

A series of parametric design studies were performed to investigate the effects of various design parameters on the bearing stiffness and overall rotordynamic performance. In order to keep the current foil gas bearing configurations (overall spring diameter and length), only the wire diameter and pitch of the springs were considered as design variables for the parametric studies. From the parametric studies, the foil gas bearing which uses the compression springs with wire diameter of 0.457mm and six coils could produce similar support stiffness comparable to that of current bump foil bearings.

Rotor-bearing orbit simulations showed there is a range of the spring stiffness for high onset speeds of the instability. Increasing the pitch of the spring increased structural loss factor slightly, manifesting a smaller number of coils is better in terms of damping. The onset speed of instability increases slightly with rotor mass due to increased static eccentricity and presumably smaller cross-coupled stiffness. However, increasing the rotor mass in order to render a high eccentricity was not very effective to increase the onset speed of instability because of reduced natural frequency and increased inertia. Instead, orbit simulations confirmed that small rotor mass with external loading is the most effective to increase the bearing stability.

# REFERENCES

[1] NASA, May 2006, *Oil Free Turbo Machinery Program,* http://www.grc.nasa.gov/WWW/Oilfree/bearings.htm

[2] Agrawal, G. L., 1997, "Foil Air/Gas Bearing Technology-An Overview," ASME Paper 97-GT-347.

[3] Costamagna, P., Magistri, L., Massardo, A.F., 2001, "Design and Part-Load Performance of a Hybrid System Based on a Solid Oxide Fuel Cell Reactor and a Micro Gas Turbine," Journal of Power Sources, **96**, pp. 352-368.

[4] Heshmat, H., Walowit, J. A., Pinkus, O., 1983, "Analysis of Gas-Lubricated Foil Journal Bearings," Journal of Lubrication Technology, **105**, pp. 647-655.

[5] Ku, C.-P., Heshmat, H., 1992, "Compliant Foil Bearings Structural Stiffness Analysis Part I: Theoretical Model-Including Strip and Variable Bump Foil Geometry," Journal of Tribology, **114**(2), pp. 394-400.

[6] Peng, J.P., Carpino, M., 1993, "Coulomb Friction Damping Effects in Elastically Supported Gas Foil Bearings," Tribology Transactions, **37**(1), pp. 91-98.

[7] Peng, J.P., Carpino, M., 1993, "Calculation of Stiffness and Damping Coefficients for Elastically Supported Gas Foil Bearings," Journal of Tribology, **115**(1), pp. 20-27.

[8] Iordanoff, I., 1999, "Analysis of an Aerodynamic Complaint Foil Thrust Bearing: Method for a Rapid Design," Journal of Tribology, **121**, pp. 816-822.

[9] Heshmat, H., 1994, ''Advancements in the Performance of Aerodynamic Foil Journal Bearings: High Speed and Load Capacity,'' Journal of Tribology, **116**, pp.287–295.

[10] DellaCorte, C., and Valco, M. J., 2000, ''Load Capacity Estimation of Foil Air Journal Bearings for Oil-Free Turbo-Machinery Applications,'' STLE Tribology Transactions, **43**(4), pp. 795–801.

[11] Dykas, B., Howard, S. A., 2004, "Journal Design Considerations for Turbomachine Shafts Supported on Foil Air Bearings," STLE Tribology Transactions, **47**, pp. 508-516.

[12] Radil, K., Howard, S., and Dykas, B., 2002, "The Role of Radial Clearance on the Performance of Foil Air Bearings," STLE Tribology Transactions, **45**(4), pp. 485–490.

[13] Kim, T., San Andrés, L., 2005, "Analysis of Gas Foil Bearings with Piecewise Linear Elastic Supports," *Proceedings of World Triboloy Congress III*, WTC 2005-63397.

[14] Kim, T., San Andrés, L., 2005, "Heavily Loaded Gas foil Bearings: A Model Anchored to Test Data," ASME Paper GT200-68486.

[15] Heshmat, H., Ku, C. -P., 1994, "Structural Damping of Self-Acting Compliant Foil Journal Bearings," Journal of Tribology, **116**(2), pp. 76-82.

[16] Rubio, D., San Andrés, L., 2005, "Structural Stiffness, Dry-friction Coefficient and Equivalent Viscous Damping in a Bump-Type Foil Gas Bearing," ASME Paper GT2005-68384.

[17] Timonshenko, S. *Strength of Materials, Part 1 and Part 2 (3rd edition)*, June 1983, Krieger Pub Co., Melbourne, Florida.

[18] Nikravesh, P. E., 1988, *Computer-aided Analysis of Mechanical Systems*, Prentice Hall., Englewood Cliffs, New Jersey.

[19] RoyMech, May 2006, Friction Factors, http://www.roymech.co.uk/Useful_Tables/Tribology/co_of_frict.htm

[20] Inman, D. J., 1995, *Engineering Vibration*, Prentice Hall., Englewood Cliffs, New Jersey.

[21] Ku, C.-P., Heshmat, H., 1993, "Compliant Foil Bearings Structural Stiffness Analysis Part II: Experimental Investigation," Journal of Tribology, **115**, pp. 364-369.

[22] Rubio, D., San Andrés, L., 2004, "Bump Type Foil Bearing Structural Stiffness: Experiments and Prediction," ASME Paper GT2004-53611.

[23] San Andrés, L., Mathcad Program: FB shaker test.mcd, Turbomachinery Laboratory, Texas A&M Uuniversity, College Station, Texas.

[24] Vance, M. J., 1987, *Rotordynamics of Turbomachinery*, John. Wiley & Son, Inc., New York.

[25] Childs, D., 1993, *Turbomachinery Rotordynamics*: *Phenomena, Modeling, and Analysis*, John. Wiley & Sons, Inc., New York.

# APPENDIX A

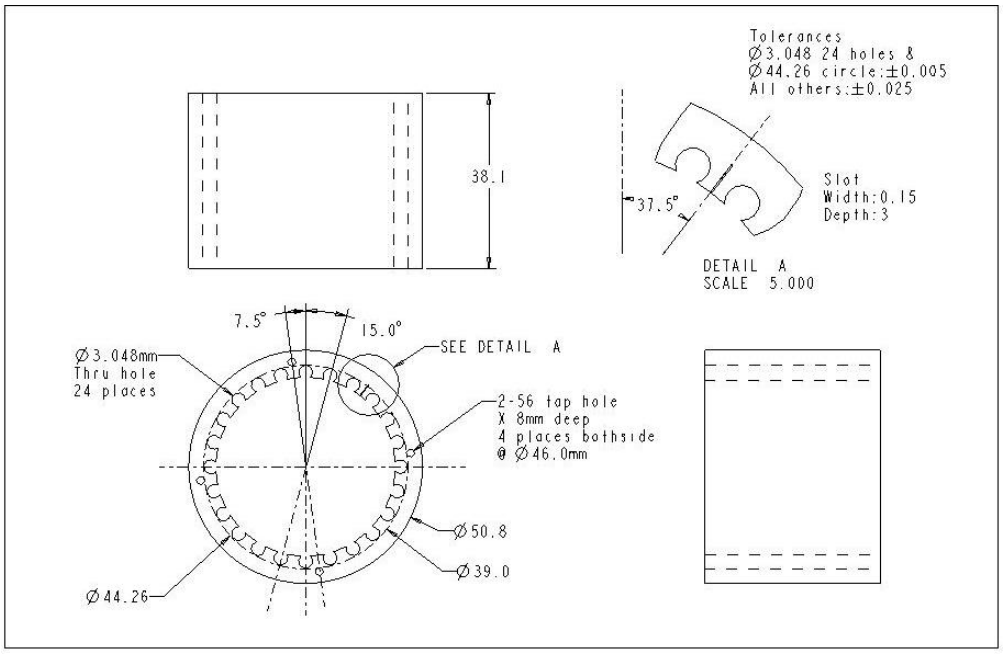


**Figure A.1 Drawing of foil gas bearing sleeve**

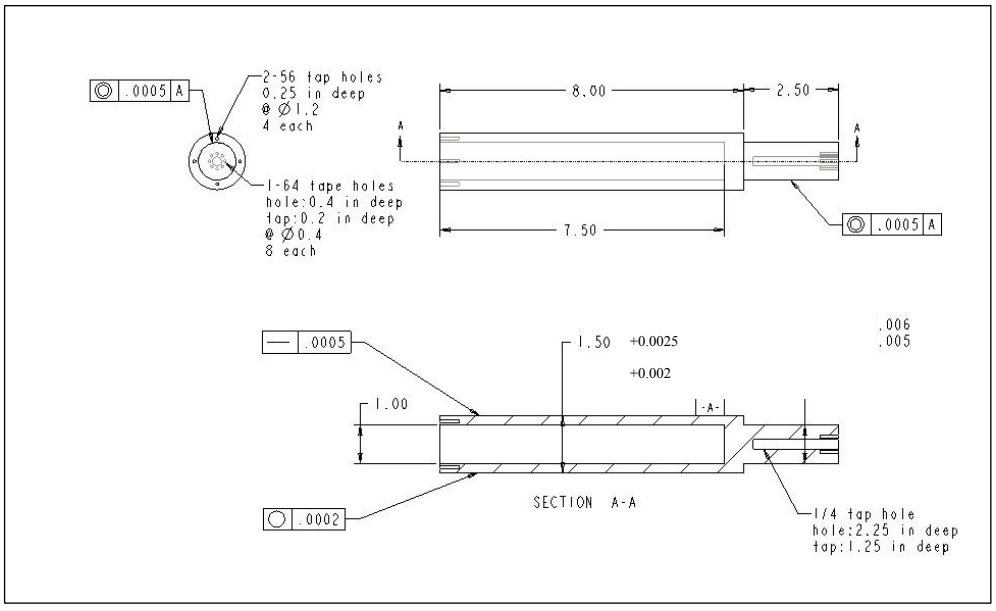


**Figure A.2 Drawing of test rotor for structural stiffness measurements**

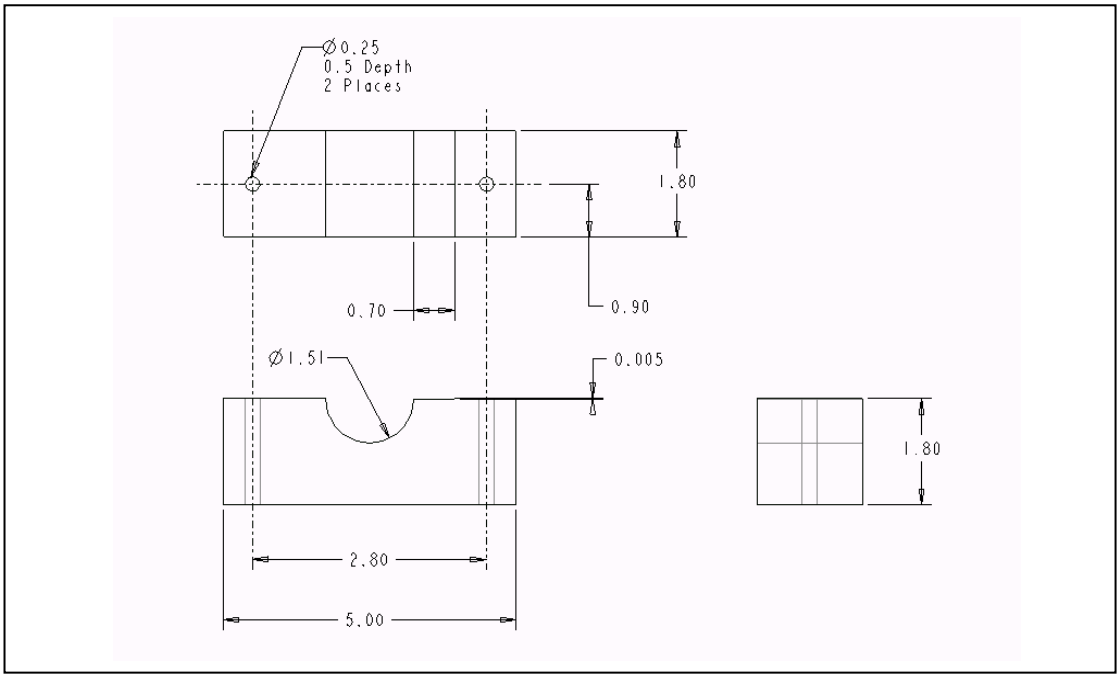


(a) Upper part of top foil forming jig

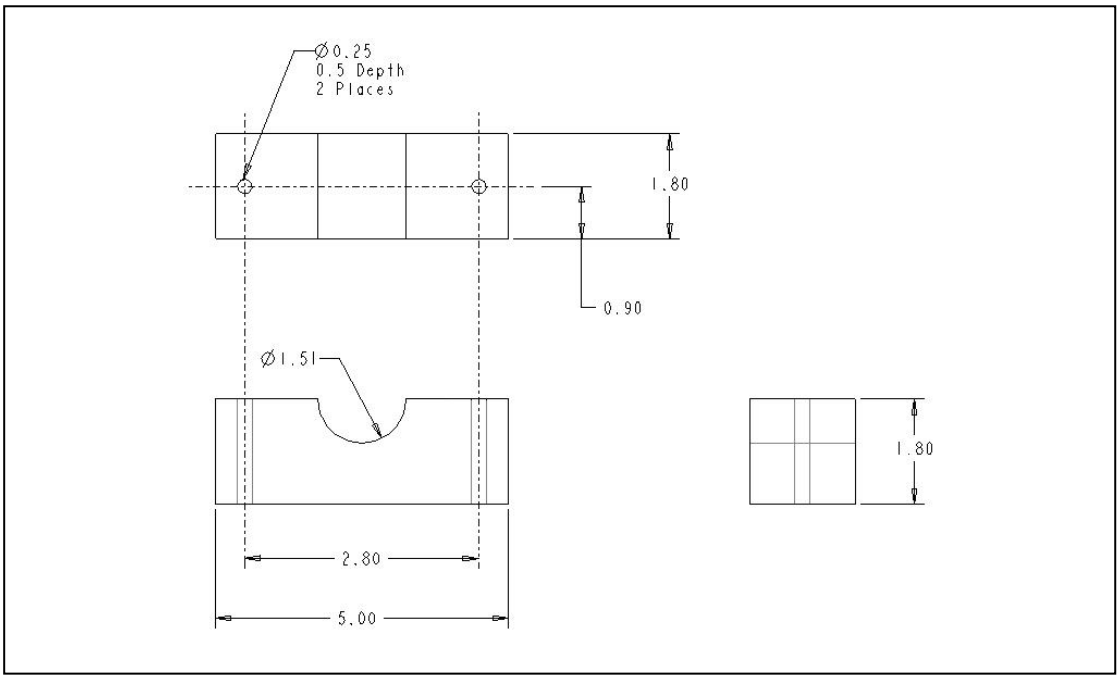


(b) Lower part of top foil forming jig

**Figure A.3 Drawing of forming jig for top foil**

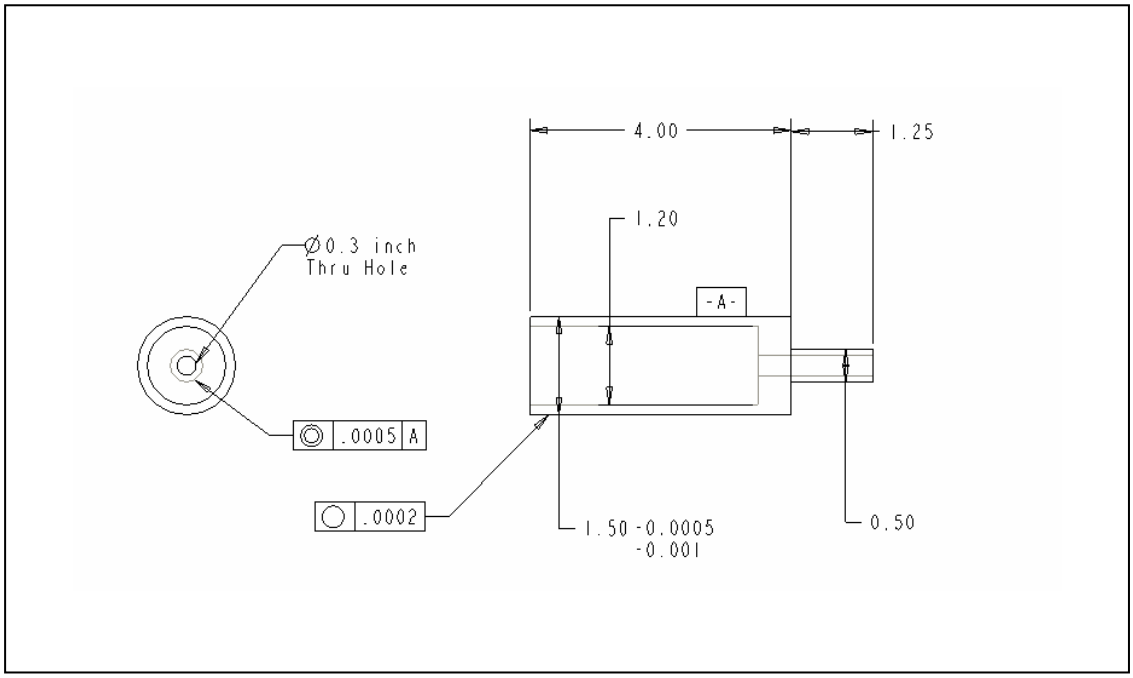


(a) Test rotor for load capacity measurements

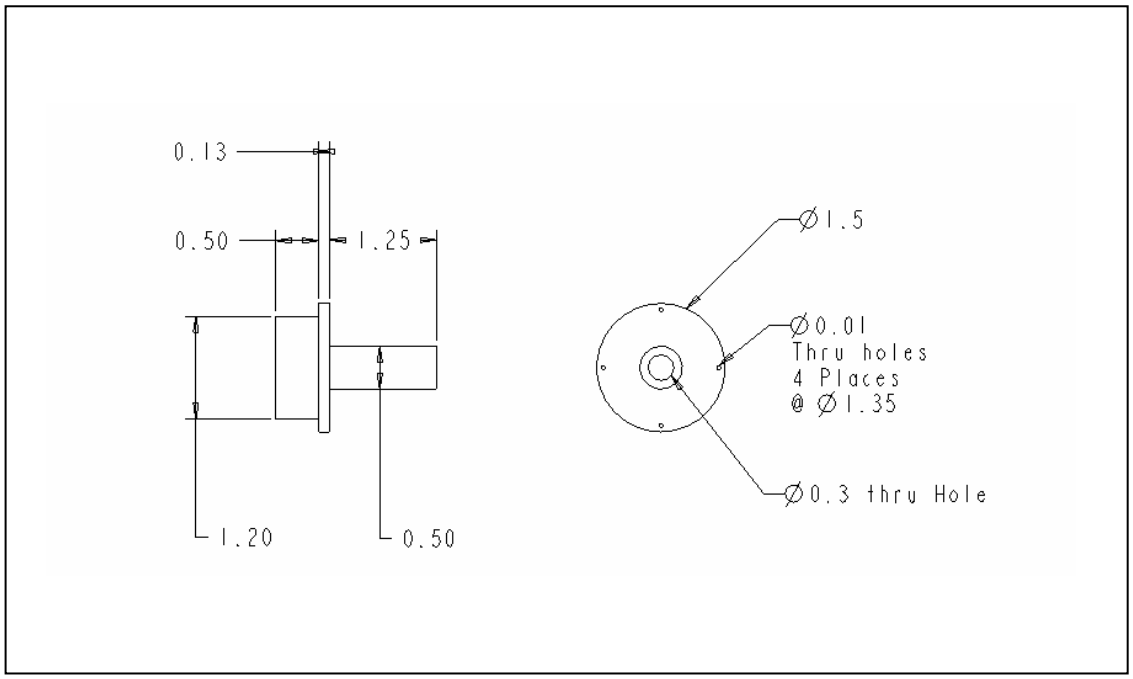


(b) Cap assembled to the test rotor for load capacity measurements

**Figure A.4 Drawing of test rotor for load capacity measurements**

**Table A.1 Specification of components for load capacity measurements**

| **Test rotor** | |
|---|---|
| Rotor length | 165.10 mm |
| Rotor diameter | 38.10 mm |
| Material | Pre-hardened 4140 steel |
| Weight | |
| **Electronic DC motor** | |
| Model | Bosch 1617EVSPK |
| Operating Range | 8,000 ( Dial 1 )~ 25,000 ( Dial 6 ) RPM |
| Max Motor Power | 2.25 HP |
| Weight | 19.5 lbs |
| **Tachometer** | |
| Model | Omega HHT13 |
| Type | Non-Contact Laser type Tachometer |
| Operating Range | 5 ~ 99,999 RPM |
| Accuracy | 0.01% of Reading |
| **Flexible coupling** | |
| Model | R+W MK2-20-44 |
| Rated Torque | 2.0 Nm |
| Operating Range | 0 ~ 25,000 RPM |
| Max. Allowable | 0.7mm (axial), 0.25mm (lateral), 2° (angular) |
| **Thermocouples** | |
| Model | Omega 5TC-KK-T-30-72 |
| Operating Range | -250 ~ 350 °C |
| Wire/Probe Diameter | 0.25mm (0.01 inch) |
| Standard Limits of Error | Greater of 1.0°C or 0.75% |

**Table A.1 Continued**

| **Temperature Display** | |
|---|---|
| Model | Omega DP 472-T-C2 |
| Display | 6 Channel, 4 digit with 0.1°C resolution |
| Accuracy | For K, J, T, E ± 1°C +0.03% RTD |
| Recording program | RS-232 |
| **Ball bearing** | |
| Model | MRC R8 FFP Single Row Deep Groove Ball Bearing |
| Dimension | 12.70 mm I.D., 28.58mm O.D., 7.94mm Width |
| Limiting Speed | 32,000 RPM |
| Load Capacity | 4.36kN for Dynamic, 2.28kN for Static Load |

# APPENDIX B

$$A_1 = 15a^2\pi^2l^2 - 6a^3\pi^4l\eta + 2a^2\pi^4l^2 - 96a^3\pi^2l\eta$$
$$A_2 = \pi^2l^4 - 9\pi^2a^2l^2 + 48\pi^2a^3l\eta - 3\pi^2al^3\eta + 24\pi^4a^4$$
$$\quad - 6\pi^4a^3l\eta + 2\pi^4a^2l^2 - 12a\eta l^3$$
$$A_3 = 30a^2\pi^2l^2 + 4a^2\pi^4l^2$$
$$A_4 = 2\pi^2l^4 - 18\pi^2a^2l^2 \ + 48\pi^4a^4 + 4\pi^4a^2l^2$$

$$C_1 = al\left(64EIa^2\pi^2 - 32GJa^2\pi^2 + 8GJl^2\right)$$
$$C_2 = al\begin{pmatrix} 8GJl^2\ (1-\beta) + 64EI\pi^2a^2(1-\beta) - 32GJ\pi^2a^2(1-\beta) + \\ \quad + 2GJa^2\pi^4(1-2\beta) + 2EIa^2\pi^4(1-2\beta) + GJl^2\pi^2(1-2\beta) \end{pmatrix}$$

$$D_1 = EI\left(10a^2l^2\pi^2 + 120a^2l^2 - 240a^2l^2\beta(1-\beta) - 32a^2l^2\pi^2\beta(1-\beta)\right)$$
$$D_2 = GJ\begin{pmatrix} 144a^2l^2\beta(1-\beta) - 384a^4\pi^2\beta(1-\beta) - 32a^2l^2\pi^2\beta(1-\beta) \\ -16l^4\beta(1-\beta) + 10a^2l^2\pi^2 + 192a^4\pi^2 - 72a^2l^2 + 5l^4 \end{pmatrix}$$

$$E_1 = -8EIa^2l\pi^2 + 4GJa^2l\pi^2 - GJl^3 + \eta\left(4EIa^3\pi^4 + GJal^2\pi^2\right)$$
$$E_2 = 8EIa^3\pi^4 + 2GJal^2\pi^2$$

$$M_1 = \left(32GJa^2l\pi^2 - 8GJl^3 - 64EIa^2l\pi^2\right)(1-\beta)$$
$$\left(-2GJa^2l\pi^4 - GJl^3\pi^2 - 2EIa^2l\pi^4\right)(1-2\beta)$$
$$+ 40EIa^3\pi^4\eta + 12GJal^2\pi^2\eta + 8GJa^3\pi^4\eta$$
$$M_2 = 32EIa^3\pi^4 + 8GJal^2\pi^2$$

$$H_1 = \left[(32\pi^2 + 240)(\beta^2 - \beta) + (10\pi^2 + 120)\right]a^2l^2$$
$$H_2 = (384\pi^2a^4 - 144a^2l^2 + 32\pi^2a^2l^2 + 16l^4)(\beta^2 - \beta)$$
$$+ 192\pi^2a^4 - 72a^2l^2 + 10\pi^2a^2l^2 + 5l^4$$

# APPENDIX C

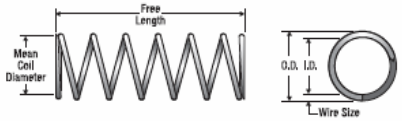


| O.D. | | CENTURY STOCK NUMBER | FREE LENGTH | | I.D. | | RATE | | SUGG. MAX. DEFL. | | SUGG. MAX. LOAD | | SOLID LENGTH | | WIRE DIA. | | TOTAL COILS | MAT'L | ENDS | FINISH |
|---|---|---|---|---|---|---|---|---|---|---|---|---|---|---|---|---|---|---|---|---|
| Inches | mm | | Inches | mm | Inches | mm | Lbs./In. | N/mm | Inches | mm | Lbs. | N | Inches | mm | Inches | mm | | | | |
| 0.120 | 3.05 | 70167S | 1.25 | 31.8 | .080 | 2.0 | 6.9 | 1.2 | .37 | 9.3 | 2.5 | 11 | .62 | 15.8 | 0.020 | 0.5 | 31.1 | SST | CG | N |
| 0.120 | 3.05 | 70186 | 1.25 | 31.8 | .076 | 1.9 | 12 | 2.1 | .42 | 11 | 5.0 | 22 | .72 | 18.2 | 0.022 | 0.6 | 32.5 | MW | CG | N |
| 0.120 | 3.05 | 70186S | 1.25 | 31.8 | .076 | 1.9 | 10 | 1.8 | .32 | 8.2 | 3.3 | 15 | .72 | 18.2 | 0.022 | 0.6 | 32.5 | SST | CG | N |
| 0.120 | 3.05 | 70204 | 1.25 | 31.8 | .072 | 1.8 | 18 | 3.1 | .35 | 9.0 | 6.4 | 28 | .77 | 19.5 | 0.024 | 0.6 | 32.0 | MW | CG | N |
| 0.120 | 3.05 | 70204S | 1.25 | 31.8 | .072 | 1.8 | 16 | 2.7 | .27 | 6.9 | 4.2 | 19 | .77 | 19.5 | 0.024 | 0.6 | 32.0 | SST | CG | N |
| 0.120 | 3.05 | 70107 | 1.38 | 35.1 | .092 | 2.3 | 1.8 | .32 | .82 | 21 | 1.5 | 6.6 | .39 | 9.9 | 0.014 | 0.4 | 27.8 | MW | CG | N |
| 0.120 | 3.05 | 70107S | 1.38 | 35.1 | .092 | 2.3 | 1.6 | .27 | .60 | 15 | .94 | 4.2 | .39 | 9.9 | 0.014 | 0.4 | 27.8 | SST | CG | N |
| 0.120 | 3.05 | 70129 | 1.38 | 35.1 | .088 | 2.2 | 2.9 | .51 | .68 | 17 | 2.0 | 8.8 | .49 | 12.5 | 0.016 | 0.4 | 30.9 | MW | CG | N |
| 0.120 | 3.05 | 70129S | 1.38 | 35.1 | .088 | 2.2 | 2.5 | .44 | .52 | 13 | 1.3 | 5.9 | .49 | 12.5 | 0.016 | 0.4 | 30.9 | SST | CG | N |
| 0.120 | 3.05 | 70151 | 1.38 | 35.1 | .084 | 2.1 | 4.6 | .81 | .61 | 15 | 2.8 | 12 | .59 | 15.0 | 0.018 | 0.5 | 32.9 | MW | CG | N |
| 0.120 | 3.05 | 70151S | 1.38 | 35.1 | .084 | 2.1 | 4.0 | .70 | .46 | 12 | 1.9 | 8.3 | .59 | 15.0 | 0.018 | 0.5 | 32.9 | SST | CG | N |
| 0.120 | 3.05 | 70169 | 1.38 | 35.1 | .080 | 2.0 | 7.0 | 1.2 | .54 | 14 | 3.8 | 17 | .70 | 17.7 | 0.020 | 0.5 | 34.9 | MW | CG | N |
| 0.120 | 3.05 | 70169S | 1.38 | 35.1 | .080 | 2.0 | 6.1 | 1.1 | .41 | 11 | 2.5 | 11 | .70 | 17.7 | 0.020 | 0.5 | 34.9 | SST | CG | N |
| 0.120 | 3.05 | 70188 | 1.38 | 35.1 | .076 | 1.9 | 11 | 1.9 | .47 | 12 | 5.0 | 22 | .78 | 19.8 | 0.022 | 0.6 | 35.5 | MW | CG | N |
| 0.120 | 3.05 | 70188S | 1.38 | 35.1 | .076 | 1.9 | 9.3 | 1.6 | .36 | 9.0 | 3.3 | 15 | .78 | 19.8 | 0.022 | 0.6 | 35.5 | SST | CG | N |
| 0.120 | 3.05 | 70073 | 1.50 | 38.1 | .100 | 2.5 | .50 | .09 | 1.1 | 28 | .55 | 2.4 | .24 | 6.0 | 0.010 | 0.3 | 23.6 | MW | CG | N |
| 0.120 | 3.05 | 70073S | 1.50 | 38.1 | .100 | 2.5 | .43 | .08 | .81 | 20 | .35 | 1.6 | .24 | 6.0 | 0.010 | 0.3 | 23.6 | SST | CG | N |
| 0.120 | 3.05 | 70089 | 1.50 | 38.1 | .096 | 2.4 | 1.0 | .18 | .94 | 24 | .94 | 4.2 | .31 | 7.8 | 0.012 | 0.3 | 25.6 | MW | CG | N |
| 0.120 | 3.05 | 70089S | 1.50 | 38.1 | .096 | 2.4 | .87 | .15 | .69 | 17 | .60 | 2.7 | .31 | 7.8 | 0.012 | 0.3 | 25.6 | SST | CG | N |
| 0.120 | 3.05 | 70108 | 1.50 | 38.1 | .092 | 2.3 | 1.7 | .30 | .85 | 22 | 1.5 | 6.6 | .40 | 10.2 | 0.014 | 0.4 | 28.8 | MW | CG | N |
| 0.120 | 3.05 | 70108S | 1.50 | 38.1 | .092 | 2.3 | 1.5 | .26 | .63 | 16 | .94 | 4.2 | .40 | 10.2 | 0.014 | 0.4 | 28.8 | SST | CG | N |
| 0.120 | 3.05 | 70130 | 1.50 | 38.1 | .088 | 2.2 | 2.7 | .48 | .72 | 18 | 2.0 | 8.8 | .52 | 13.2 | 0.016 | 0.4 | 32.5 | MW | CG | N |
| 0.120 | 3.05 | 70130S | 1.50 | 38.1 | .088 | 2.2 | 2.4 | .42 | .55 | 14 | 1.3 | 5.9 | .52 | 13.2 | 0.016 | 0.4 | 32.5 | SST | CG | N |
| 0.120 | 3.05 | 70152 | 1.50 | 38.1 | .084 | 2.1 | 4.2 | .73 | .67 | 17 | 2.8 | 12 | .65 | 16.6 | 0.018 | 0.5 | 36.3 | MW | CG | N |
| 0.120 | 3.05 | 70152S | 1.50 | 38.1 | .084 | 2.1 | 3.6 | .63 | .51 | 13 | 1.9 | 8.3 | .65 | 16.6 | 0.018 | 0.5 | 36.3 | SST | CG | N |
| 0.120 | 3.05 | 70170 | 1.50 | 38.1 | .080 | 2.0 | 6.5 | 1.1 | .59 | 15 | 3.8 | 17 | .75 | 19.1 | 0.020 | 0.5 | 37.6 | MW | CG | N |
| 0.120 | 3.05 | 70170S | 1.50 | 38.1 | .080 | 2.0 | 5.6 | .98 | .45 | 11 | 2.5 | 11 | .75 | 19.1 | 0.020 | 0.5 | 37.6 | SST | CG | N |
| 0.120 | 3.05 | 70189 | 1.50 | 38.1 | .076 | 1.9 | 9.7 | 1.7 | .51 | 13 | 5.0 | 22 | .86 | 21.7 | 0.022 | 0.6 | 38.9 | MW | CG | N |
| 0.120 | 3.05 | 70189S | 1.50 | 38.1 | .076 | 1.9 | 8.4 | 1.5 | .39 | 10 | 3.3 | 15 | .86 | 21.7 | 0.022 | 0.6 | 38.9 | SST | CG | N |
| 0.120 | 3.05 | 70205 | 1.50 | 38.1 | .072 | 1.8 | 15 | 2.6 | .43 | 11 | 6.4 | 28 | .92 | 23.2 | 0.024 | 0.6 | 38.1 | MW | CG | N |
| 0.120 | 3.05 | 70205S | 1.50 | 38.1 | .072 | 1.8 | 13 | 2.3 | .33 | 8.3 | 4.2 | 19 | .92 | 23.2 | 0.024 | 0.6 | 38.1 | SST | CG | N |

# VITA


| | |
|---|---|
| Name: | Ju Ho Song |
| Address: | Department of Mechanical Engineering, 3123, TAMU, College Station, Texas, USA. |
| Email: | windreams@hotmail.com |
| Education: | B.S., Mechanical Engineering, Korea University, Korea, 2003<br>M.S., Mechanical Engineering, Texas A&M University, USA, 2006 |